Rapid Solidification and Non-equilibrium Phase Constitution in Laser Powder Bed Fusion (LPBF) of AlSi10Mg Alloy: Analysis of Nano-precipitates, Eutectic Phases, and Hardness Evolution

HONG QIN, QINGSHAN DONG, VAHID FALLAH, and MARK R. DAYMOND

The non-equilibrium phase evolution during laser powder bed fusion (LPBF) of AlSi10Mg alloy is thoroughly characterized and analyzed by means of advanced electron microscopy and analytical simulation of rapid solidification phenomenon. The evolution of microstructural strengthening agents such as inter-cellular eutectic phase and intra-cellular precipitates is presented in correspondence with the local variation of cellular/dendritic solidification patterns within a typical melt pool. The eutectic phase exhibits two different morphologies: lamellar and fibrous. As with the cell size variation, the overall volume fraction of eutectic phase and the lamella spacing is shown to gradually decrease by moving away from the melt-pool boundary (MPB), *i.e.*, through crossing over from a coarse to a fine cellular zone. The eutectic-free regions within the α-Al cells contain a large number density of nano-sized precipitates that are predominantly Si-rich and are either fully or semi-coherent with the Al matrix. The formation of nano-precipitates is linked to the increased (non-equilibrium) solubility limits of α-Al cells due to the rapid solidification effect. For the first time, we identify such nano-precipitates with non-equilibrium crystal structures and morphologies: ''Spheres'' and ''Ellipsoids'' with Face Centered Cubic (FCC), and ''Plates'' and ''Needles'' with a Diamond Cubic (DC) superlattice structure that emerges from within the Al matrix. The microstructure in the heat-affected zone (HAZ) right underneath the MPB exhibits an absence of cell boundaries and eutectic phases while consisting primarily of large Si-rich and Mg-rich precipitates. Finally, the local variation of nano-hardness across a solidified melt pool is shown to correlate well with the corresponding profile of microstructural refinement, *i.e.*, exhibiting a minimum at the HAZ and a peak at around the melt-pool centerline. The findings here can significantly advance the state of knowledge for the strengthening behavior in an as-built LPBF-processed AlSi10Mg alloy.

https://doi.org/10.1007/s11661-019-05505-5

I. INTRODUCTION

HYPO-EUTECTIC and eutectic Al-Si alloys (*e.g.,* 7 to 12 wt pct Si) are attractive choices of materials for weight-saving metal 3D printing applications. While possessing a low density (~ 2.7 g/cm^3), these alloys exhibit relatively high strength and strain hardening capacity in the as-built (as-printed) state.[1] This is mainly owing to a high degree of microstructural refinement that can be achieved in these alloys *via* solidification under high cooling rates.[1–4] Cooling rates as high as 10^6 Ks^{-1} have been found to exist during Laser Powder Bed Fusion (LPBF)[3,5] (as opposed to much lower cooling rates attainable *via* conventional casting processes, *e.g.*, ~ 300 Ks^{-1} in strip casting of Al alloys[6]). At such high cooling rates, non-equilibrium solidification patterns can evolve in hypo-eutectic Al-Si alloys.[5,7–9] Sarreal and Abbaschian[7] showed that, at a cooling rate of 10^6 K s^{-1}, the volume fraction of eutectic phase and the α-Al solubility limit largely deviate from the equilibrium values (*i.e.*, as determined by the equilibrium Al-Si phase diagram). The same rapid solidification phenomena and the corresponding phase evolution were reported by Marola *et al.*[4] to occur in an LPBF-processed AlSi10Mg alloy. The apparent effect of such non-equilibrium solidification conditions on the resulting microstructure can be observed in the results of a recent study by Qin *et al.*[2] which investigated the microstructural evolution in a LPBF-processed

HONG QIN, QINGSHAN DONG, VAHID FALLAH, and MARK R. DAYMOND are with the Department of Mechanical and Materials Engineering, Queen's University, Kingston, ON K7L 3N6, Canada. Contact e-mails: qingshan.dong@queensu.ca; vahid.fallah@queensu.ca
Manuscript submitted April 9, 2019.
Article published online November 1, 2019

AlSi10Mg alloy. They revealed an exceptionally refined cellular/dendritic structure in which the α-Al cells contain nano-sized precipitates while the cell boundary regions accommodate pockets of eutectic lamellae as well as precipitates.

LPBF of AlSi10Mg alloy has been extensively studied in the past few years with a focus on process optimization for higher mechanical properties in the builds.[*e.g.*, 1,10–15] A few of the more recent studies have attempted to explain the observed process-dependency of mechanical properties by means of characterization and analysis of microstructural evolution during LPBF. Xiong *et al.*[10] have addressed the ambiguous dependency of tensile properties to the build direction. This was done by correlating the change in the mechanical properties (due to the build direction) to the corresponding distribution of melt-pool boundaries with respect to the load-bearing face of the printed tensile specimens. Through analysis of fracture surfaces, they suggested the weak and vulnerable melt-pool boundaries to be the main cause of failure, the orientation of which determines the strength and ductility as a function of build direction (*i.e.*, either horizontal or vertical). Therefore, they ruled out the significance of solidification microstructure and texture. During the analysis of mechanical properties, however, one should also investigate the effect of the evolution of primary strengthening agents in the microstructure, *e.g.*, cell boundaries, eutectic lamellae, and precipitates in AlSi10Mg alloy. The significant impact of such microstructural features on the deformation behavior has been emphasized in a recent study by Hadadzadeh *et al.*[1] They investigated the response of the as-built microstructure to dynamic loading in an attempt to explain the complex deformation mechanisms of LPBF-processed AlSi10Mg alloy. In the process, the evolution of dislocation networks and low-angle grain boundaries was explained in relation to the distribution of cell boundaries, eutectic lamellae, and precipitates.

To date, despite being extensively investigated for novel weight-saving AM applications, AlSi10Mg alloy has not been thoroughly analyzed as to reveal and explain the evolution of the microstructural strengthening agents under LPBF processing conditions. To be able to draw an accurate map of process-microstructure-property relationships, it is imperative to understand the mechanisms controlling the evolution of cells/dendrites, eutectic lamellae, and precipitates. Here, following the lead from our recent observations of phase constitution in an LPBF-processed AlSi10Mg alloy,[2] the evolution of nano-precipitates and size and volume fraction of eutectic lamellae within a solidified melt pool are characterized by means of state-of-the-art (analytical and experimental) Transmission Electron Microscopy (TEM) techniques. Furthermore, through analytical simulation of rapid solidification phenomenon, in the context of LPBF processing conditions, we shed light on underlying mechanisms controlling the phase evolution. Finally, the nano-hardness variations across the microstructure will be explained in relation to the evolution of the strengthening agents.

II. EXPERIMENTAL PROCEDURE

An AlSi10Mg powder starting stock with a size range of 20 to 63 μm and an Mg content of approximately 0.3 wt pct was used in this study. An optical micrograph of the cross-sectional view of the powder particles is shown in Figure 1(a). The powders were printed into a rectilinear sample (100 mm × 20 mm × 10 mm) on a support structure of 3 mm in height, as shown in Figure 1(b). The sample was printed in an Ar atmosphere using a Renishaw AM400 (equipped with a Y fiber laser operated in pulse mode) run with the machine's default parameters listed in Table I. The build plate was heated to a temperature of 35 °C during printing and a hatching angle of 67 deg, counter-clockwise (see Figure 1(b)), was employed between consecutive layers to enhance the densification of the finished part, as explained in Reference 2.

Samples for metallographic analysis were prepared in the front-view cross section (in the vicinity of the *XZ* plane in Figure 1(b)) by sectioning along the building direction (*Z*) of the as-fabricated part. The samples were ground to #2000 SiC paper and then mechanically polished with 3 μm diamond suspension followed by a final fine-polishing using 0.6 μm colloidal silica slurry. All samples were ion-milled using a PECS II system before performing Scanning Electron Microscopy (SEM). Melt track morphology and cellular/dendritic structure were characterized using a FEG-SEM (FEI Nova NanoSEM 400) at 20 kV, operated in secondary electron imaging mode. For nano-hardness measurements across, a specimen was prepared in the top-view cross section (in the vicinity of the *XY* plane in Figure 1(b)) and then polished and ion-milled with the same procedure as described above. The nano-hardness was measured using NanoTest Vantage system with a Berkovich indenter under depth-control mode. In order to reveal the hardness evolution across the solidified melt pool, 6 (rows) × 6 indents (totaling 36) with a loading and unloading rate of 2.0 mN/s and a depth of 1500 nm were applied.

For Transmission Electron Microscopy (TEM) experiments, 3-mm-diameter discs from the front-view section (in the vicinity of the *XZ* plane in Figure 1(b)) were ground down to ~ 70 μm which were then ion-milled using a PIPS II system. A fully digital 200 kV FEI Tecnai Osiris (Scanning) Transmission Electron Microscope (S/TEM) was used for a comprehensive microstructural, crystal structure/orientation, and chemical composition analysis in nano-to-atomic scale. The four Super-X windowless Energy Dispersion X-ray (EDX) detectors incorporated in the TEM allowed for fast acquisition of X-ray spectrum and a high sensitivity for low-energy counts, and also enabled nano-scale mapping of elemental distribution using Chemi-STEM EDX technology. The acquisition and post-acquisition data processing were carried out by Bruker's ESPRIT Microanalysis Software. The mapping setup varies with the thickness of the sample and the spot size of the STEM beam, as the intensity of X-ray depends on the thickness and the beam current. To obtain more accurate chemical distribution maps, it is necessary to

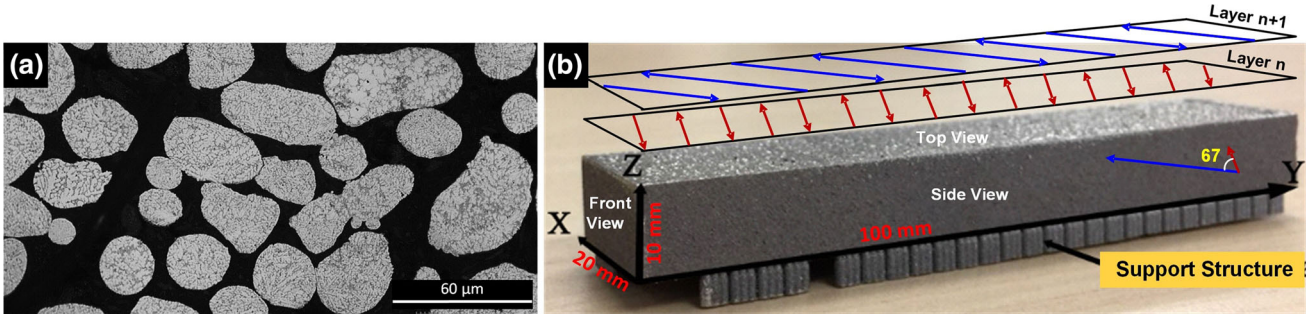

Fig. 1—(*a*) Optical micrograph of a cross-sectional view of AlSi10Mg powder starting stock and (*b*) the printed sample with schematic representation of scanning strategy.

Table I. LPBF Processing Parameters

Laser Power (W)	Exposure Time* (s)	Point Distance* (m)	Velocity (m/s)	Layer Thickness (m)	Beam Diameter (m)	Hatch Spacing (m)
275	0.00004	0.00008	2	0.00003	0.00007	0.00008

*Energy is transmitted *via* a fiber optic cable and delivered using a point-by-point exposure methodology.

increase the dwell time as long as possible. In order to acquire high-resolution TEM (HRTEM) images and micro-diffraction patterns of nano-precipitates, the viewing area was selected within a region as thin as possible, *e.g.*, regions by the very edge of the polishing hole. A 10-nm condenser aperture (C2) enabled the detection of the diffraction patterns of features as small as 5 nm by Microprobe without inserting a selective aperture. The identification of crystal orientation relationship between the aluminum matrix and Si-rich precipitates was based on micro-diffraction patterns which were analyzed with the assistance of CaRIne Crystallography software. To obtain higher quality images for a more accurate quantitative analysis, the Higauss filter in Image-Pro® Plus software was applied to the EDX Si composition maps, *e.g.*, for estimation of eutectic lamella spacing. Image J software was used for the estimation of eutectic volume fraction in the EDX images by imposing the default thresholding method (*i.e.*, by adjusting the brightness values until only the eutectic phase is revealed) and analysis of area percentage. A fast Fourier transform (FFT) was applied to the HRTEM images (including the whole map area) to acquire the diffraction patterns using Image J software.

III. RESULTS

The as-deposited microstructure is investigated below by means of electron microscopy and image processing in order to comprehensively characterize the evolution of eutectic phases and precipitates.

A. *Solidification Structure*

The evolution of solidification structure throughout the cross section (Figure 2(a)), as well as within a single solidified melt pool (Figures 2(a_1–a_2)), is revealed by secondary electron SEM images. A randomly distributed repetitive cusp-like pattern across the front view can be observed in Figure 2(a_1). The 67 deg rotation of scanning direction of each consecutive layer, together with a varying (unsteady) depth of the melt pool penetrating into previous layers, is suggested as the main factors accounting for such randomization.[2] Each solidified melt pool is clearly profiled by a melt-pool boundary (MPB). The higher magnification image in Figure 2(a_1) reveals the cellular/dendritic microstructure across two neighboring melt pools, where three distinguishable zones can be identified: a fine zone, a heat-affected zone (HAZ), and a coarse zone. The typical width of the HAZ is estimated to be 3.41 ± 0.81 μm. It can be seen that the coarse zone and the HAZ are separated by the MPB. The comprehensive solidification mechanisms, patterns, and sequences upon which these zones evolve under LPBF processing conditions have been thoroughly investigated and explained in a separate study by the authors.[2] More detailed microstructural features of the three zones can be observed in a higher magnification image shown in Figure 2(a_2); *i.e.*, the eutectic phases are detectable within the cell boundaries in both fine and coarse zones while, in the HAZ, only large-sized individual particles can be observed. It can be seen that there is a difference in eutectic lamella size and volume fraction between the coarse and fine zones. This is further confirmed with the bright-field TEM images shown in Figures 2(b) and (b_1) to (b_3) which more clearly reveal the distribution of eutectic phases and precipitates within various zones. The images shown in Figures 2(b_1) to (b_3) reveal that fine and coarse zones contain precipitates that are finer and appear with different morphologies than those in the HAZ. The eutectic phase, as can be seen in Figures 2(b_1) and (b_2), appears predominantly with a lamellar morphology. However, in addition, there are coarse particles residing intermittently along the cell boundaries which

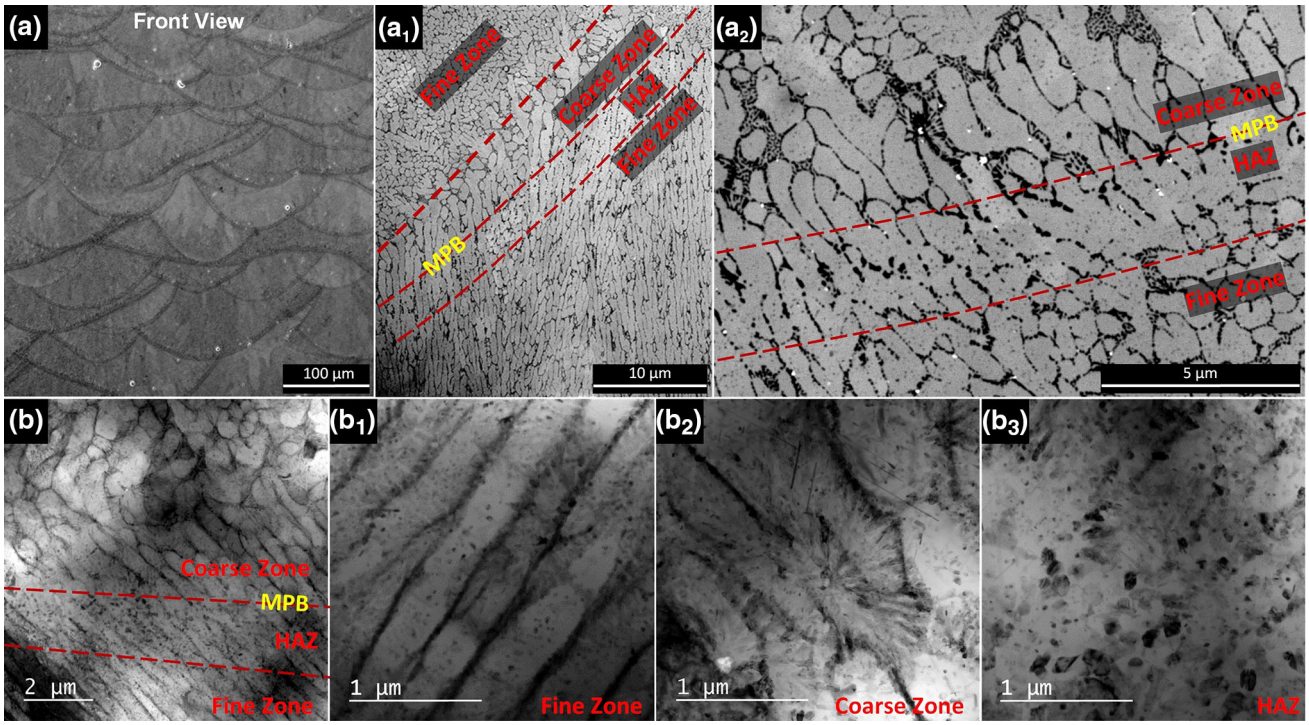

Fig. 2—The evolution of solidification microstructure within the front-view cross section as well as within one solidified melt track is shown in (a_{1-3}) secondary SEM images and (b) a bright-field TEM image obtained at 2 deg from $[100]_{Al}$ zone axis along (110) plane; each melt track can be divided into three major zones as shown in the bright TEM images: (b_1) coarse, (b_2) fine, and (b_3) HAZ. Note: the coarse zone and HAZ are separated by the melt-pool boundary, MPB.

can be indicative of a fibrous eutectic phase. Also, it seems there exists a higher volume of coarser eutectic phases in the coarse zone than in the fine zone, the extent of which will be quantitatively investigated below.

Figure 3 shows EDX chemical composition maps for Si, Mg, and O obtained in $[110]_{Al}$ zone axis in the fine zone, the coarse zone, and the HAZ. It can be seen that, within the fine and coarse zones, the main solute elements, Si (Figures 3(a_1) and (b_1)) and Mg (Figures 3(a_2) and (b_2)), are concentrated along the cell boundaries, forming Si/Mg-rich inter-cellular networks. It is also apparent that there exist a high number density of sub-micron oxygen-rich particles (Figures 3(a_3) and (b_3)) across the microstructure. From the superimposition of noise-filtered O concentration maps on the Si concentration maps shown in Figures 3(a_4) and (b_4), it appears that the oxygen-rich particles reside within the cell boundaries as well as in the vicinity of eutectic lamellae and particles in both fine and coarse regions. It can be suggested that these oxygen-rich particles are oxide phases that have existed in the solid form throughout the solidification process. They, then, have been pushed away by the moving solid/liquid (S/L) interface during solidification finally residing where the last stage of solidification occurs, *i.e.*, around the cell boundaries. At oxygen levels that are normally present in the atmosphere of LPBF processing chambers, it has been shown that oxidation of aluminum alloys is inevitable and oxide scales form within intra-track and inter-layer interfaces.[3,16,17] The laser beam breaks through these oxide layers upon depositing the subsequent layers.[16,17] As a result, the broken-up oxide scales float in the melt pool and will be trapped within the solidification microstructure. A closer look at the compositional maps in higher magnification suggests that these oxygen-rich particles represent oxide phases of various nature, *i.e.*, Si-, Mg-, and/or Al-rich. Determining the exact origin and further characterization and identification of the various oxide phases observed here can be the subject of a future study.

From the magnified Si concentration maps shown in Figures 3(a_5) and (b_5), it can be seen that the eutectic lamellae structure is noticeably coarser in the coarse region than in the fine region, while it has disappeared and been replaced with coarse Si-rich precipitates in the HAZ (Figure 3(c_5)). The large Si-rich precipitates in the HAZ exhibit a morphology and size distribution that are consistent with those forming due to heat treatment of LPBF-processed AlSi10Mg.[18] Upon a solution treatment at 450 °C for 2 hours, Li *et al.*[18] have shown that a network of Si-rich particles precipitates out of the Al matrix replacing the original eutectic network. The eutectic lamella spacing was estimated using the intercept method on the Si concentration maps (after being processed with Higuass filter image analysis in Image Pro® software for a clearer distinction of lamellae). The analysis, performed on ten different regions representing either fine or coarse zones, showed a variation of an

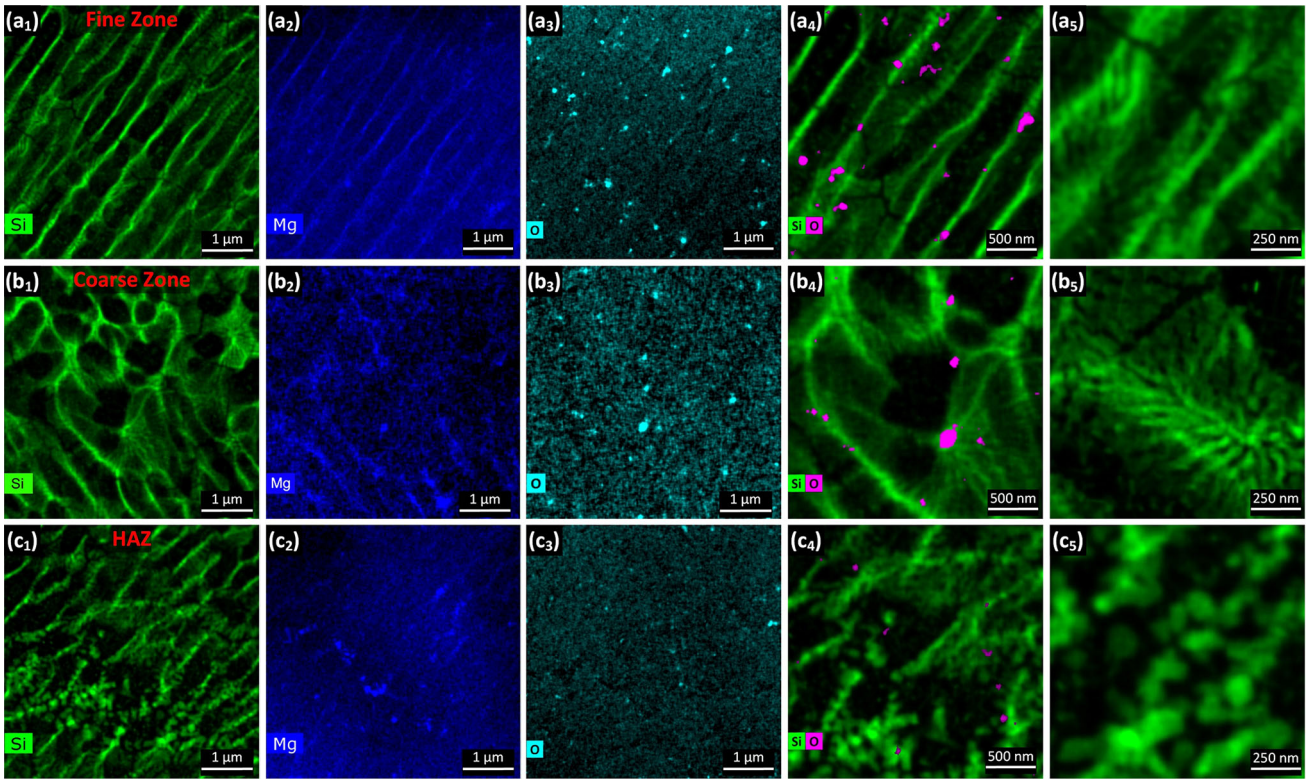

Fig. 3—The EDX chemical composition maps for (a_1) to (a_3) the fine zone, (b_1) to (b_3) the coarse zone, and (c_1) to (c_3) the HAZ obtained in $[110]_{Al}$ zone axis; (a_4, b_4, c_4) noise-filtered oxygen maps are superimposed on the Si maps in (a_1), (b_1), and (c_1) with twice as large a magnification. The magnified views of the Si concentration maps reveal a eutectic lamellar structure within (a_5) the fine and (b_5) the coarse zones, and (c_5) a network of large Si-rich particles in the HAZ.

average spacing of 80.08 ± 2.3 nm and 67.8 ± 1.8 nm in the coarse and fine zones, respectively. The estimation of the overall volume fraction of eutectic phases (using ImageJ software on the same sets of Si concentration maps), however, indicates a reduction from 84.8 ± 0.72 pct to 78.2 ± 0.36 pct from coarse to fine region. It is noticeable that the eutectic lamellae and cell boundaries have disappeared in the HAZ, as can be seen in Figure 3(c_5). It seems the Si/Mg-rich inter-cellular networks have broken up into large precipitates distributed around the original cell boundaries. Figure 4 shows the high magnification views of cells representative of fine and coarse zones as well as a typical HAZ microstructure. For a clearer view of the precipitates, the cells with relatively low eutectic content are chosen. In eutectic-free regions within the cells, phases primarily consist of nano-scale Si-rich precipitates of various morphologies and orientations, as confirmed by both the STEM-HAADF contrast (Figures 4(a_1) and (b_1)) and Si and Mg concentration maps (Figures 4(a_2) to (a_3), (b_2), and (b_3)). Moreover, the STEM-HAADF contrast and concentration maps of the HAZ (Figures 4(c_1) to (c_3)) indicate that the large-sized precipitates are rather distinctively Si- or Mg-rich in nature. This resembles the results of a post-LPBF heat treatment procedure (*i.e.,* solution treatment at 520 °C) which causes co-precipitation of the Mg_2Si phase with Si precipitates in an AlSi10Mg alloy.[19]

B. *Nano-precipitates*

From the microstructural analysis in the previous section, we can see that a large number of nano-sized precipitates (that are predominantly Si-rich in nature) have nucleated in the eutectic-free areas within the α-Al cells (such as those observed in the Si concentration maps shown Figures 4(a_2) and (b_2)). The morphology and orientation of these precipitates seem to vary from one to another as well as from the fine to the coarse zone and the HAZ. These precipitates could act as effective strengthening agents along with the eutectic lamellae and cell boundaries. Therefore, in order to understand the effect of LPBF process variables (and thus the local solidification conditions and cooling rates) on the evolution of microstructure and local and bulk mechanical properties, it is imperative to identify these precipitates, *i.e.*, in terms of their morphology, crystal structure, orientation relationship, and coherency with the matrix. There have been a few studies on the precipitation behavior of these alloys under LPBF conditions (*e.g.*,[20]) where Si-rich precipitates have been simply referred to as Si particles without any further investigation into their crystal structure, morphology, and/or compositional evolution. Acknowledging the lack of such information in the published literature, below we present our thorough investigation and characterization of the evolution of nano-sized Si-rich precipitates under high cooling rates during LPBF.

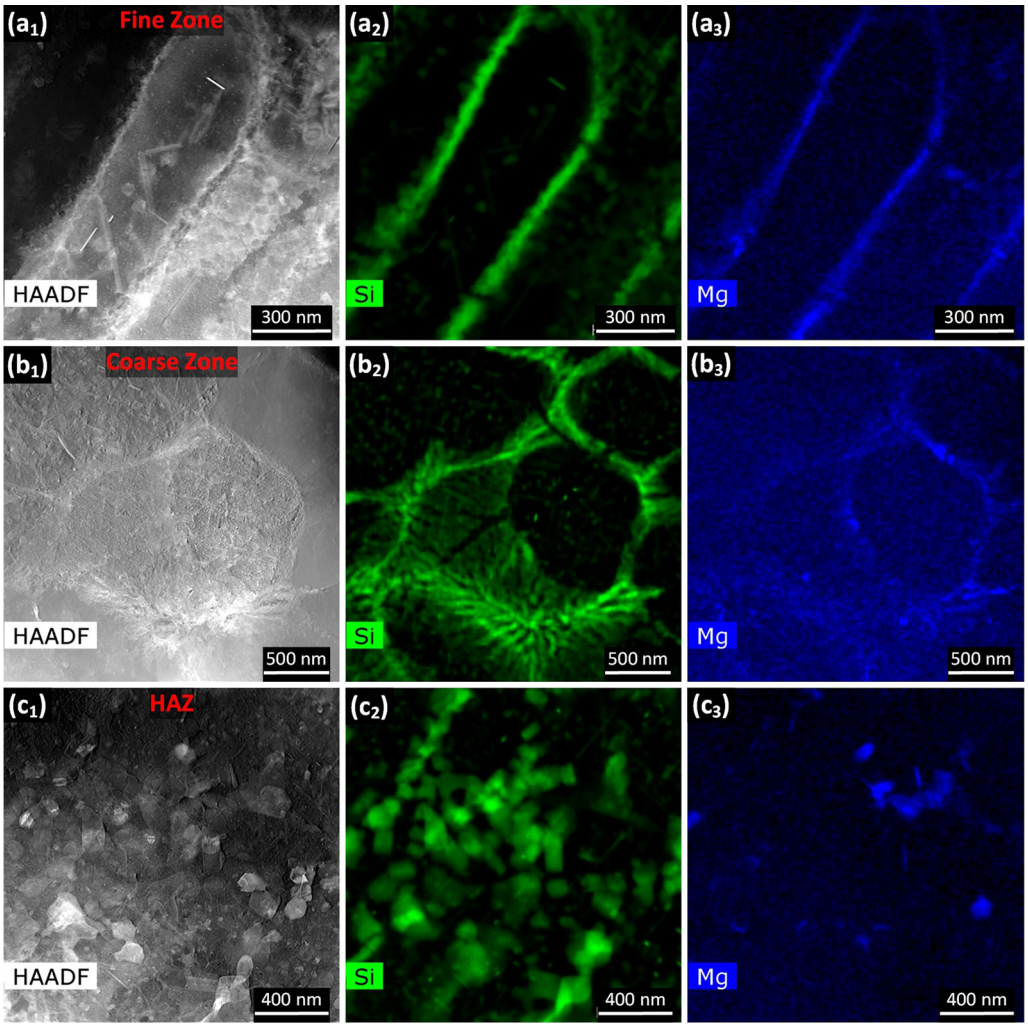

Fig. 4—STEM-HAADF images in $[100]_{Al}$ zone axis and the corresponding EDX Si and Mg concentration maps of a cell within ($a_{1–3}$) the fine zone, ($b_{1–3}$) the coarse zone and ($c_{1–3}$) the HAZ.

Figures 5(a_1), (a_2), (b_1), and (b_2) show a single cell within the fine zone imaged in $[100]_{Al}$ and $[110]_{Al}$ zone axes, respectively, with both STEM-HAADF and Si concentration color contrast. The magnified views of the Si concentration color maps, shown in Figures 5(a_3) and (b_3), reveal that the Si-rich precipitates appear with either an elongated or non-elongated morphology. The elongated precipitates appear all with a large aspect ratio in both $[100]_{Al}$ and $[110]_{Al}$ zone axes which is indicative of a needle-like morphology. The needles are categorized into three groups according to their elongation direction: *i.e.*, referred to as "Needle⟨112⟩," "Needle⟨110⟩," and "Needle⟨100⟩" hereafter (as labeled in Figures 5(a_3) and (b_3)). It is noticeable that different variants of needle⟨110⟩ and needle⟨100⟩ can be observed in both $[100]_{Al}$ and $[110]_{Al}$ zone axes, while needle⟨112⟩ appears only in $[110]_{Al}$ zone axis in a relatively lower number density compared to the other two. It is believed that Bragg's condition for needle⟨112⟩ is met only in $[110]_{Al}$ zone axis, which indicates these needles may possess a different crystal structure and/or a different orientation relationship with the Al matrix. The non-elongated precipitates can be observed in both zone axes appearing either with a relatively spherical (referred to as either "Spheres" or "Ellipsoids," hereafter) or with a faceted morphology (referred to as "Plates," hereafter). Therefore, one can categorize the precipitates within the α-Al cells on the basis of the following major aspects: (1) crystal structure, (2) morphology, and (3) orientation relationship with the Al matrix. As presented below, detailed crystallographic information will be obtained from various precipitates identified in Figures 5(a_3) and (b_3) using an analysis of micro-diffraction patterns (acquired in the TEM mode) as well as a complimentary HRTEM imaging and analysis.

1. *Spheres and ellipsoids*

The HRTEM imaging of spheres and ellipsoids, as shown in Figure 6, suggests that their size may vary from a few nanometers to over ~ 30 nm in diameter. It is noteworthy that the finer spheres and ellipsoids are visible only in the HRTEM images. As can be inferred from the higher magnification image of the small spherical precipitates (Figure 6(c)) and the larger

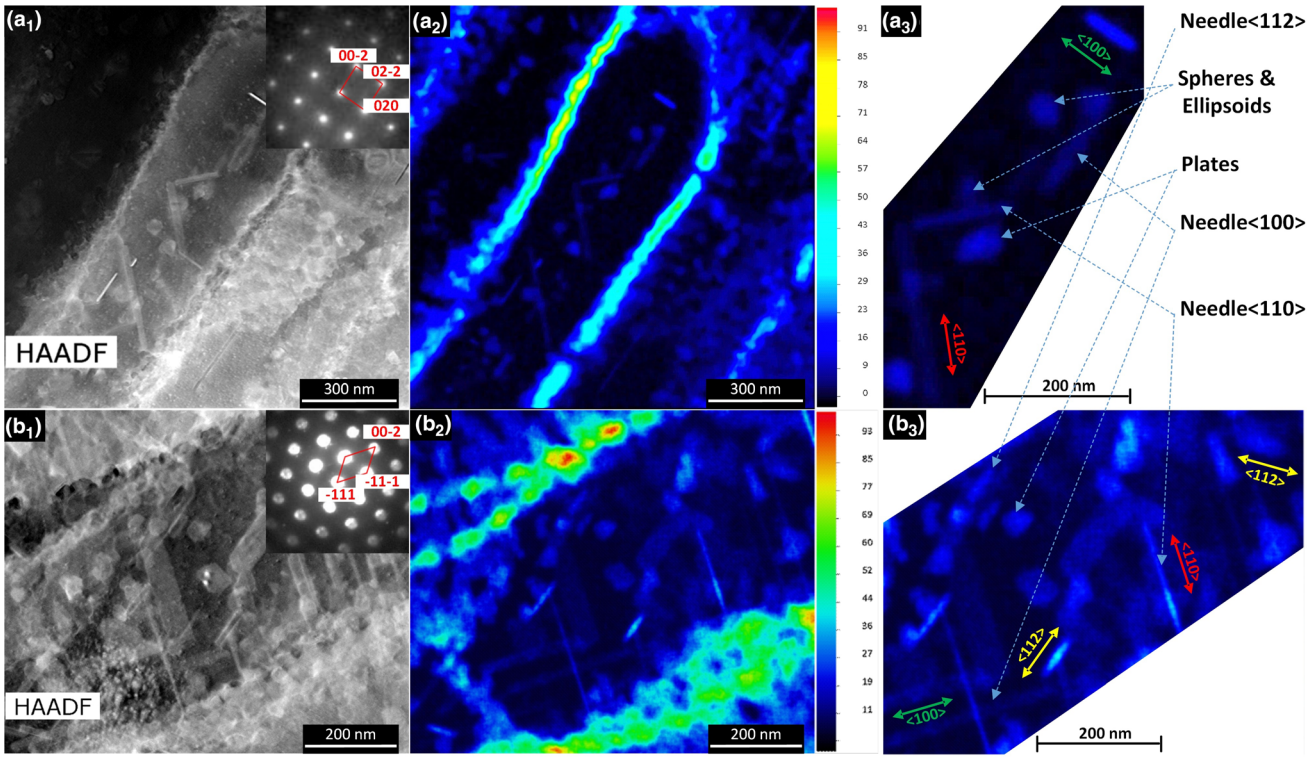

Fig. 5—Si-rich nano-precipitates revealed in the fine zone in STEM-HAADF images and EDX Si concentration maps obtained in ($a_{1–2}$) $[100]_{Al}$ and ($b_{1–2}$) $[110]_{Al}$ zone axes. Examples of different types of Si-rich precipitates are labeled in (a_3) and (b_3) that show the magnified views of the precipitates in (a_2) and (b_2), respectively. The Si concentration in the EDX images above is represented with a color map.

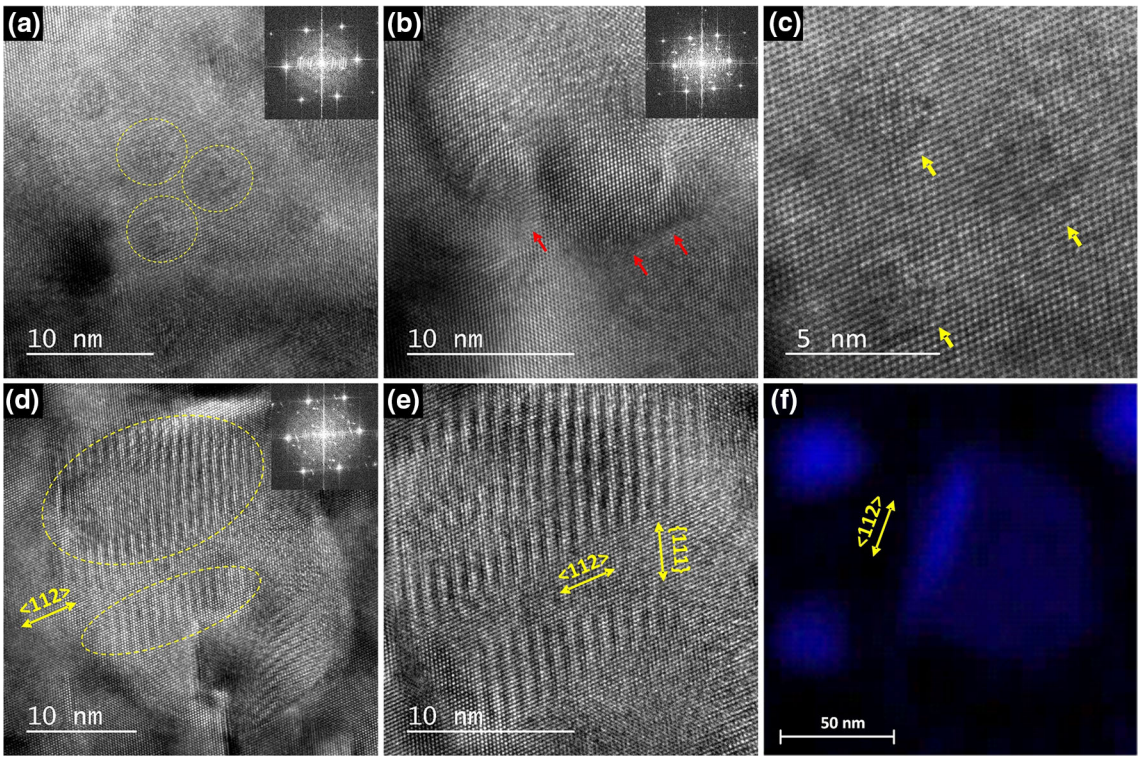

Fig. 6—Spherical and ellipsoidal Si-rich precipitates revealed in HRTEM images obtained in $[110]_{Al}$ zone axis: (*a*) and (*b*) Small and large spherical Si-rich precipitates, respectively, and (*c*) the magnified view of small spherical Si-rich precipitates in (a); (*d*) ellipsoidal Si-rich precipitates and (*e*) their magnified view; (*f*) a magnified view of the spherical and ellipsoidal Si-rich precipitates from an EDX Si concentration map obtained in $[110]_{Al}$ zone axis. The arrows in (b) point to the locations of some misfit dislocations.

spherical precipitate (shown in Figure 6(b)), spheres are fully coherent and share the same crystal structure with the matrix. The larger spherical precipitate is, however, accompanied by misfit dislocations at discrete areas along its interface with the matrix (as labeled by arrows in Figure 6(b)). It is believed that the spherical precipitates are slightly enriched in Si, the content of which is thought sufficient to cause noticeable lattice displacements. Similarly, as can be inferred from the HRTEM images shown in Figures 6(d) and (e), the precipitates with ellipsoidal morphology are fully coherent with the matrix and possess the same crystal structure as the matrix. It can be seen, however, that the ellipsoids are elongated along ⟨112⟩ directions while also showing a uniform lattice displacement of {111} atomic planes along their long axis. The magnified snapshot of an EDX Si concentration map (shown in Figure 6(f)) further confirms the morphology and orientation of spheres and ellipsoids as well as their coexistence within the α-Al matrix. The crystallographic characteristics of spheres and ellipsoids are consistent with those observed by Fallah *et al.* during early-stage precipitation in AA6000 series (AlMgSi)[21–23] and AA2000 (AlCu)[24,25] alloys. In both systems, early precipitates/clusters were identified with either a spherical or an elongated morphology possessing the same crystal structure as of the Al matrix with slightly distorted lattice structures.[21–25] Moreover, a variant of elongated early precipitates/clusters were shown to be elongated in ⟨112⟩ directions (stretched along {111} planes[21,22,24,25] which was shown to be an energetically favorable orientation for the initial transition from spherical to an elongated morphology.[22,24] It is thus suggested that, in the AlSi10Mg system, the spheres may act as the precursor phase to those that have evolved into ellipsoids.

2. *Plates*

The HRTEM image shown in Figure 7(a) reveals the atomic structure of a plate-like precipitate. The lower half of the precipitate exhibits a distinct atomic arrangement manifesting the emergence of a Diamond Cubic (DC)-like superlattice crystal structure from within the Al matrix. The micro-diffraction patterns obtained from multiple plates in both $[110]_{Al}$ and $[100]_{Al}$ zone axes (shown in Figures 7(b) and (c), respectively) confirm the DC-like arrangement of atomic planes within the plates. Within the DC portion of the precipitate, the precipitate/matrix interface seems to be coherent. Also, the DC lattice is oriented along the same zone axis as that of the Al matrix, suggesting an orientation relationship of $\langle 110\rangle_{DC}//\langle 110\rangle_{Al}, \{\bar{1}11\}_{DC}//\{\bar{1}11\}_{Al}$. The upper half of the plate, however, does not exhibit a clear atomic arrangement though remaining coherent with the Al matrix. In fact, all plates observed under HRTEM exhibited a partially distorted nature, *i.e.*, a mixed DC/undefined (distorted) crystal structure as in Figure 7(a).

3. *Needle⟨112⟩*

The HRTEM images (Figures 8(a_1) and (b_1)) and corresponding inverse FFTs (Figures 8(a_2) and (b_2)) of

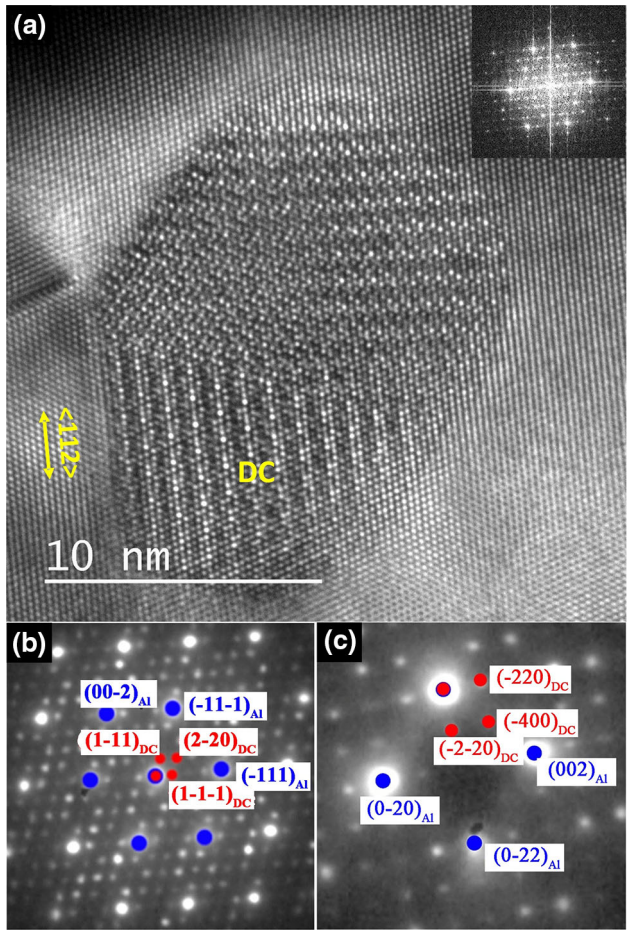

Fig. 7—(*a*) HRTEM image showing a plate-like Si-rich precipitate revealed in $[110]_{Al}$ zone axis, along with (*b*) and (*c*) micro-diffraction patterns in $[110]_{Al}$ and $[100]_{Al}$ zone axes, respectively, obtained from plate-like features identified in Fig. 5(a_3) and (b_3).

needle⟨112⟩ precipitates reveal an atomic structure that, similar to that in plates, resemble a DC-like superlattice crystal structure. The corresponding FFTs (Figures 8(a_3), (b_3), (c_1) to (c_3)) represent a diffraction pattern that resembles that of a DC crystal structure in $[114]_{DC}$ zone axis. It should be noted that a combination of relative distances and angles between the reflection spots were employed to identify the zone axis of the corresponding DC diffraction pattern; *e.g.*, the relative distances of $R_{\{\bar{3}\bar{1}1\}}/R_{\{\bar{2}20\}} = 1.190$, $\varphi = 71$ deg from the FFT was found reasonably consistent with the standard value of $R_{\{\bar{3}\bar{1}1\}}/R_{\{\bar{2}20\}} = 1.173$, $\varphi = 64.76$ deg from the $[114]_{DC}$ zone axis. Accordingly, the orientation relationship between the Al matrix and needle⟨112⟩ was determined as $\langle 114\rangle_{DC}//\langle 110\rangle_{Al}, \{\bar{2}20\}_{DC}//\{\bar{1}11\}_{Al}$. Similar to the plates, consistently across the microstructure, needle⟨112⟩ was found to be partially distorted, *i.e.*, possessing a mixed DC/undefined(distorted) crystal structure. In contrast, however, the zone axis of DC superlattice crystal structure within the needle⟨112⟩ is rotated with respect to that of the Al matrix, *i.e.*, $[114]_{DC}$ *vs* $[110]_{Al}$. As a result, the interface between the needle⟨112⟩ and the Al matrix appears to be

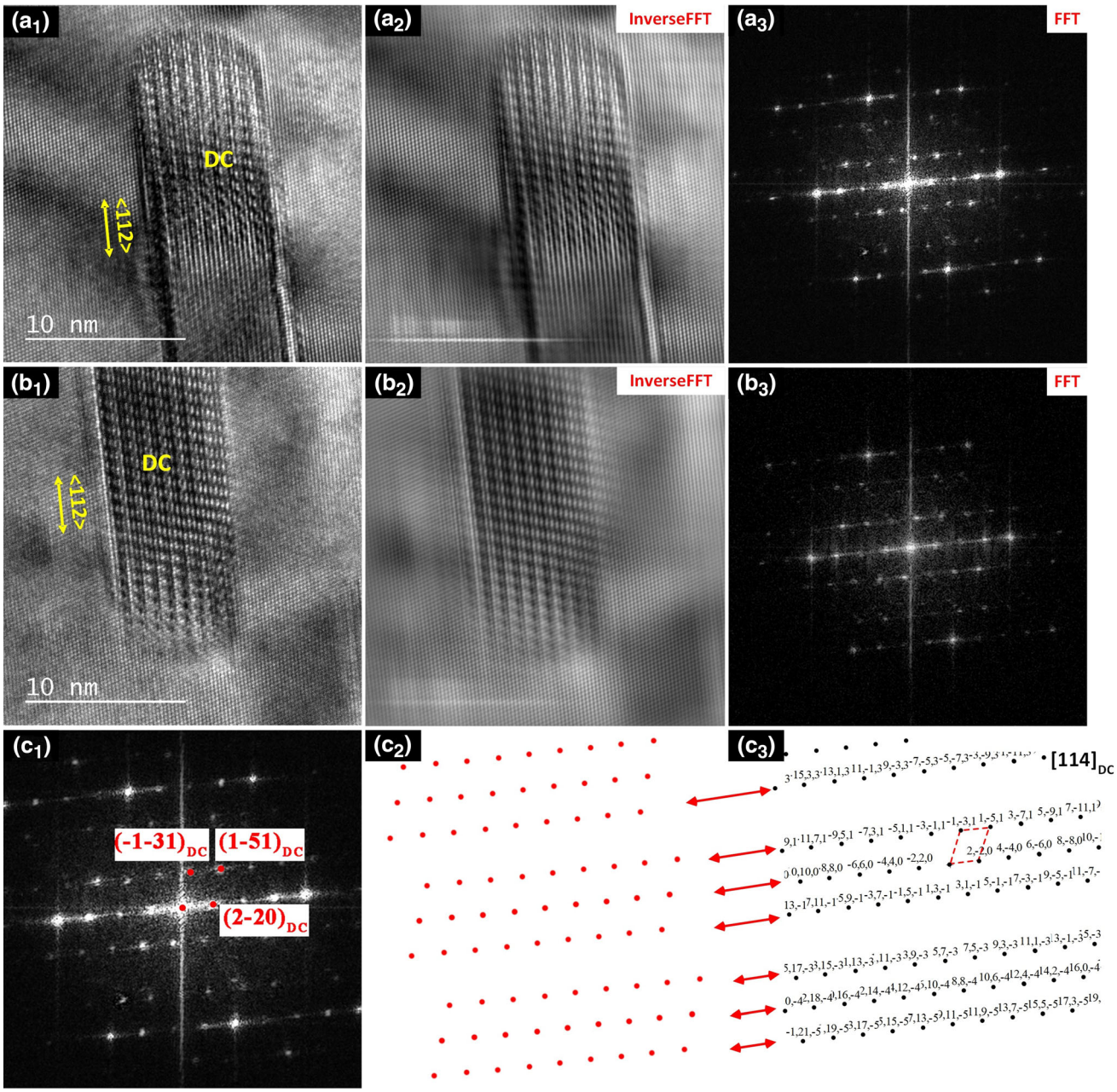

Fig. 8—(a_1) and (b_1) Needle-like Si-rich precipitates, needle⟨112⟩, revealed in the HRTEM image in $[110]_{Al}$ zone axis, along with the corresponding (a_2) and (b_2) inverse FFT and (a_3) and (b_3) FFT, and (c_1) and (c_3) the DP indexing for a typical DC crystal structure in $[114]_{DC}$ zone axis. c_1 is an enlarged view of a_3 and c_2 is the extracted DPs from c_1 for better visibility.

semi-coherent (*i.e.*, coherent along the length and incoherent across the width of the needle).

It should be emphasized that, due to the highly non-equilibrium nature of these needles, every needle⟨112⟩ phase observed in the microstructure exhibited distorted lattice structures partly along its long axis. This made it very difficult for quality imaging and thus obtaining a clear FFT for needle⟨112⟩. However, with the resemblance demonstrated in Figure 8 below, it can be concluded with high confidence that needle⟨112⟩ has a DC-like crystal structure.

4. *Needle⟨110⟩*

As demonstrated in Figures 9(a) and (b), using the methodology described above, a typical micro-diffraction pattern of needle⟨110⟩ (obtained in $[100]_{Al}$ zone axis) is matched with the standard DC diffraction pattern in $[114]_{DC}$. Accordingly, the orientation relationship with the matrix is determined as $\langle 114\rangle_{DC}//\langle 100\rangle_{Al}$, $\{\bar{3}\bar{1}1\}_{DC}//\{02\bar{2}\}_{Al}$. It is noteworthy that two rows of diffraction spots are missing from the standard DC diffraction pattern (indicated by dotted lines in Figure 9(b)) which correspond to the forbidden

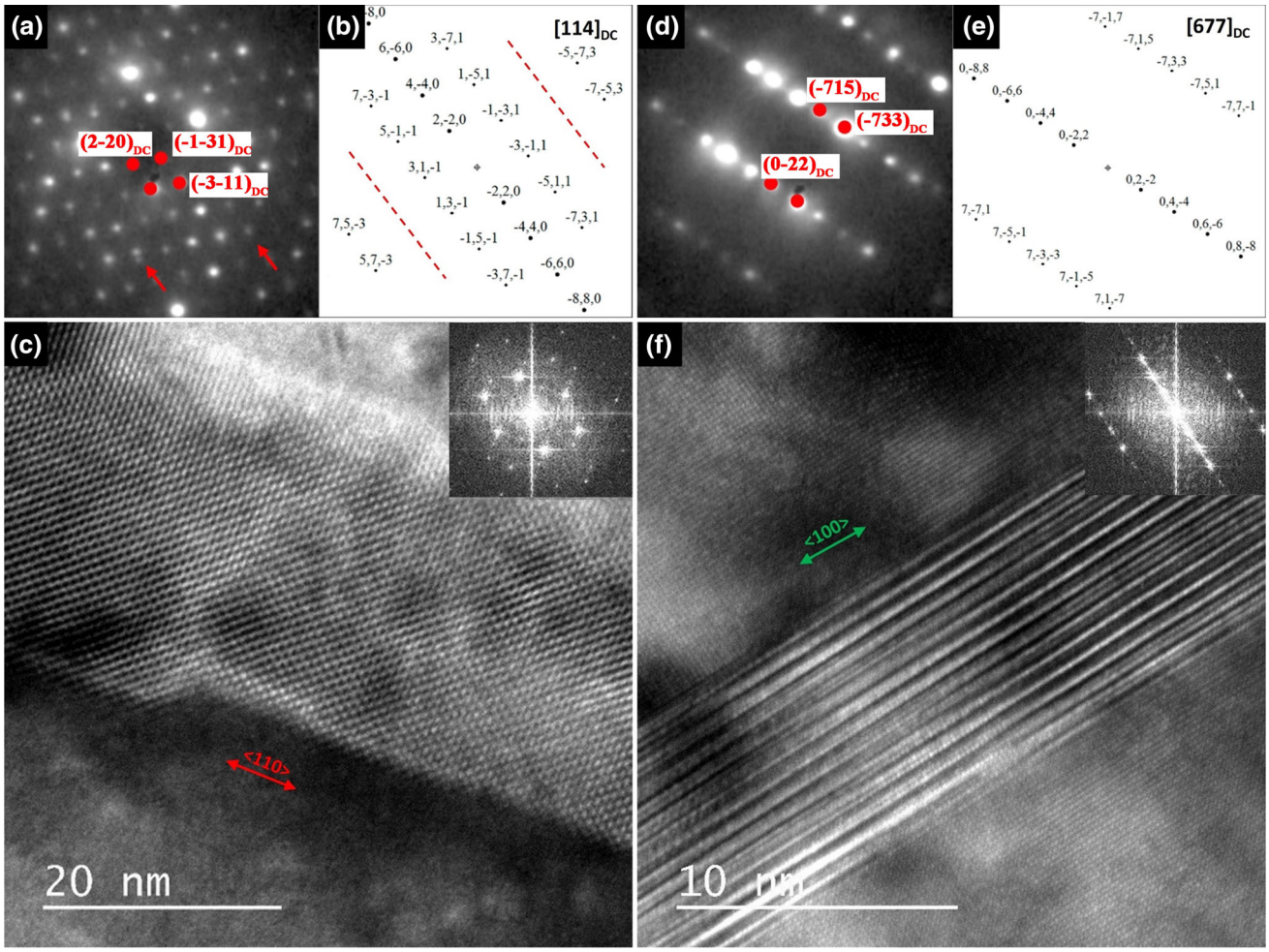

Fig. 9—Needle⟨110⟩ and needle⟨100⟩ identified with micro-diffraction patterns and HRTEM imaging in $[100]_{Al}$ zone axis: (*a*) to (*c*) needle⟨110⟩ micro-diffraction pattern, a typical diffraction pattern for DC structure in $[114]_{DC}$ zone axis and the corresponding HRTEM image, respectively; (*d*) to (*f*) needle⟨100⟩ micro-diffraction pattern, a typical diffraction pattern for DC structure in $[677]_{DC}$ zone axis and the corresponding HRTEM image, respectively.

reflections in $[114]_{DC}$ zone axis (*i.e.*, $|F_s|^2 = 0$, where F_s is the structure factor of Si). The appearance of these rows in the micro-diffraction pattern of the needle⟨110⟩ (arrowed in Figure 9(a)) may be attributed to the fact that the needle contains not only Si but also Al and Mg atoms, due to which the Bragg's condition may be met for the crystal planes representing the forbidden reflections in Si. From the micro-diffraction pattern shown in Figure 9(a) (that exhibits some overlapping reflection spots with those of the Al matrix) and the HRTEM image shown in Figure 9(c), it can be suggested that needle⟨110⟩ is semi-coherent with the Al matrix.

5. *Needle⟨100⟩*

Figures 9(d) and (e), respectively, show the micro-diffraction pattern of a typical needle⟨100⟩ and the matching diffraction pattern that can be obtained from a standard DC crystal structure in $[677]_{DC}$ zone axis. The orientation relationship is then determined as $\{\bar{7}33\}_{DC}//\{002\}_{Al}, \langle 677\rangle_{DC}//\langle 100\rangle_{Al}$. Similar to needle⟨110⟩, needle⟨100⟩ also appears to be semi-coherent with the Al matrix, *i.e.*, coherent across the width and incoherent along the length of the needle (as can be inferred from the HRTEM image shown in Figure 9(f) and the inset FFT).

Both needle⟨110⟩ and needle⟨100⟩ were frequently observed with either a partially or a fully distorted/faulted lattice structure across the microstructure. Figures 10(a) and (c) show examples of fully distorted/faulted variants of needle⟨110⟩ and needle⟨100⟩, respectively. Needle⟨100⟩, as shown in Figure 10(b), often appears with a DC superlattice crystal structure that contains a high number density of dislocations aligned in the same direction while being uniformly distributed across the needle. These dislocations create a unique strain contour that appears as stripes across the width of the needles. Table II summarizes the important characteristics of various Si-rich precipitates identified within the α-Al cells in the fine region.

The same types of precipitates as found in the fine zone could be identified within the α-Al cells in the coarse zone after examining both $[100]_{Al}$ and $[110]_{Al}$ zone axes. There is, however, an apparent increase in the

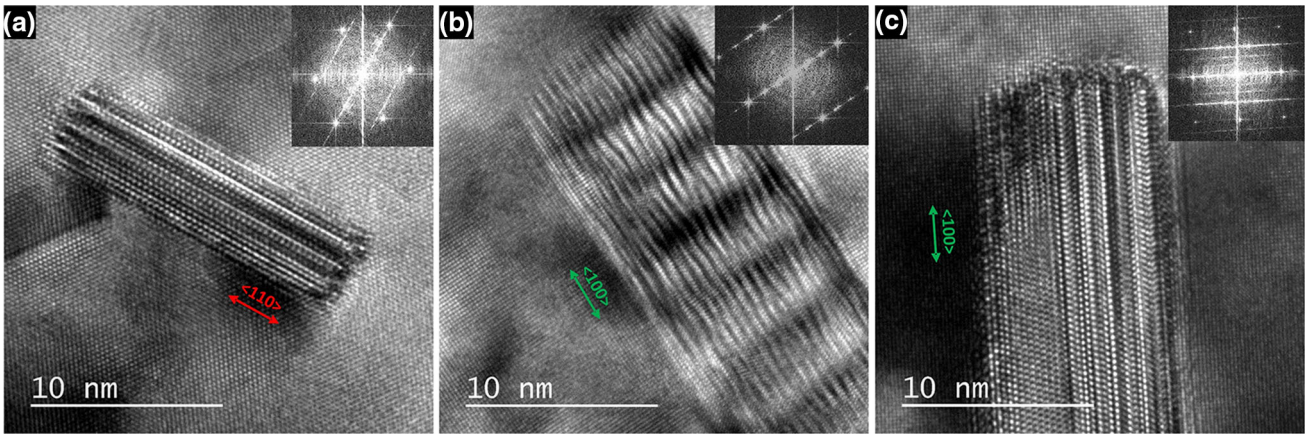

Fig. 10—HRTEM images of needles with irregular/distorted lattice structures; (*a*) needle⟨110⟩ observed in $[110]_{Al}$ zone axis and (*b*) and (*c*) needle⟨100⟩ observed in $[100]_{Al}$ zone axis. The needle ⟨100⟩ shown in (b) exhibits a DC-like crystal structure with strain contours created by numerous dislocations that are aligned in one direction and at regular intervals.

Table II. Characteristics of Si-Rich Nano-precipitates Identified Within the α-Al Cells in the Fine Region

Precipitate	Orientation	Crystal Structure	Orientation Relationship with Matrix	Interface Coherency
Sphere	—	FCC	—	coherent
Ellipsoid	⟨112⟩	FCC	—	coherent
Plate	—	DC superlattice	$\langle 110\rangle_{DC}//\langle 110\rangle_{Al}$ $\{-111\}_{DC}//\{-111\}_{Al}$	coherent
Needle⟨112⟩	⟨112⟩	DC superlattice	$\langle 114\rangle_{DC}//\langle 110\rangle_{Al}$ $\{-220\}_{DC}//\{-111\}_{Al}$	semi-coherent
Needle⟨110⟩	⟨110⟩	DC superlattice	$\langle 114\rangle_{DC}//\langle 100\rangle_{Al}$ $\{-3-11\}_{DC}//\{02-2\}_{Al}$	semi-coherent
Needle⟨100⟩	⟨100⟩	DC superlattice	$\langle 677\rangle_{DC}//\langle 100\rangle_{Al}$ $\{-733\}_{DC}//\{002\}_{Al}$ $\{-0-22\}_{DC}//\{0-20\}_{Al}$	semi-coherent

number density of needle⟨100⟩ precipitates as compared with the fine zone (as can be inferred from the bright-field TEM image and the corresponding EDX Si concentration maps shown in Figures 11(a) and (b), respectively, compared with those of the fine zone (shown in Figure 5)). Carrying out image analysis on the EDX Si concentration maps in $[100]_{Al}$ zone axis (obtained from ten different regions of each zone), it was estimated that needle⟨100⟩ exhibits a number density of ~ $28 \times 10^6/mm^2$ and ~ $53 \times 10^6/mm^2$ in the fine zone and the coarse zone, respectively. It can be suggested that needle⟨100⟩ is further stabilized in the coarse zone than in the fine. This may be due to the fact that, as presented by Qin *et al.*,[2] lower cooling rates are present in this zone compared with the fine zone.

IV. DISCUSSION

Here we investigate the mechanisms upon which the eutectic phase and the nano-precipitates evolve across the solidified melt pools. The evolution of such phases which, along with the cell boundaries, contributes to the strength of AlSi10Mg alloy will be linked to the corresponding variation of nano-hardness across the microstructure.

A. *Eutectic lamella spacing*

As explained in Section III–A, the eutectic lamellar structure exhibits a variation of an average spacing of 80.08 ± 2.3 nm and 67.8 ± 1.8 nm in the coarse and fine zones, respectively. In fact, the eutectic lamellae seem to be gradually refined from the coarse region towards the fine region, the variation of which can be explained in correlation with the local cooling rate. The variation of solidification cooling rate, ε, can be estimated from the local values of the solidification velocity, V_s, and temperature gradient, G, along the S/L interface, *i.e.*, $\varepsilon = V_s G$. Due to the very small sizes of the melt pool in LPBF, the variations in G within the S/L interface (obtained from numerical simulations) are rather negligible and often reported in the literature as a constant value (*e.g.*, ~ 10^6 Km^{-1}[3]). The change in the cooling rate along the S/L interface is thus primarily controlled by V_s variations. The V_s, on the other hand, has been

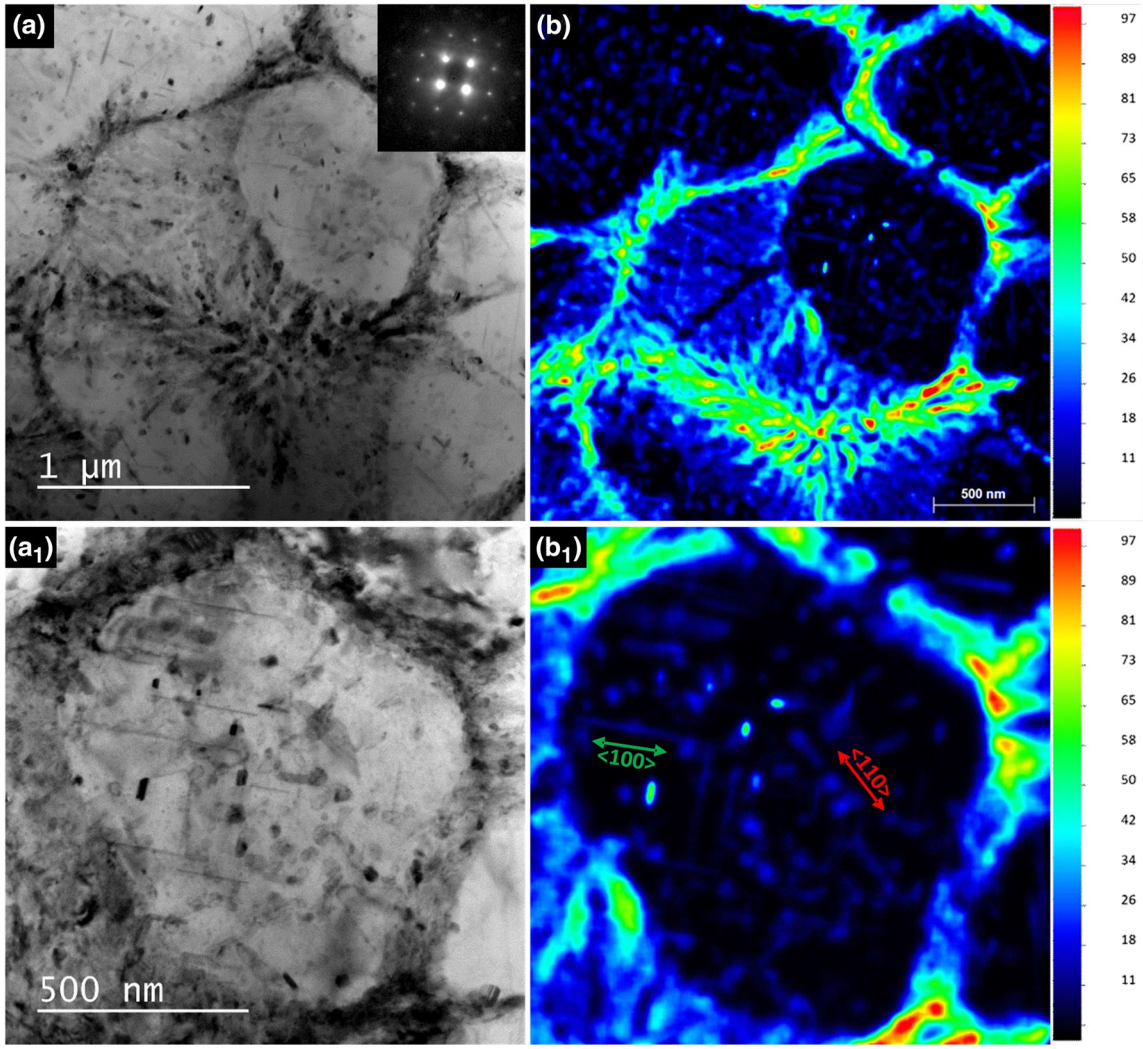

Fig. 11—Nano-precipitates revealed within the α-Al cells in the coarse zone; (*a*) the bright-field image and (*b*) the corresponding EDX Si concentration map obtained in $[100]_{Al}$ zone axis. (a_1) and (b_1) show the magnified views of one cell from the images in (a) and (b), respectively.

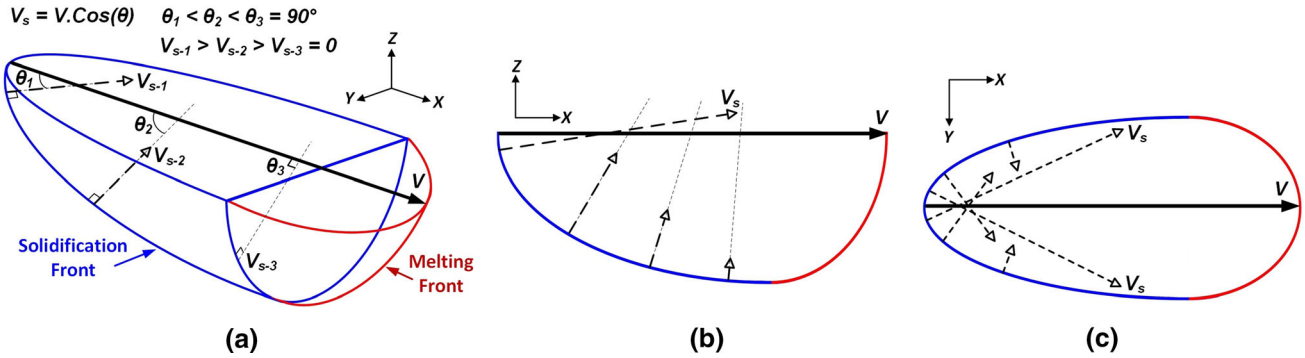

Fig. 12—(*a*) Schematic representation of the melt-pool shape and geometry during LPBF. The variation of solidification velocity, V_s, relative to the beam scan velocity, V is depicted as a function of location along the S/L interface; (*b*) schematic evolution of V_s within a vertical section around mid-width of the melt pool; (*c*) schematic evolution of V_s within a horizontal section around mid-depth of the melt pool.

shown to be primarily determined by the S/L interface morphology for solidification of a predominantly cellular structure (*e.g.*, in the absence of extensive side branches) which is constrained by the fast motion of the laser beam.[2,26,27] The cellular/dendritic structure thus grows predominantly along the normal to the S/L interface meaning $V_s = V\cos\theta$, where V is the laser scan velocity vector and θ is the angle between the normal to

the S/L interface and the laser scan direction. A more detailed explanation can be found in Reference 2. Figure 12(a) shows a schematic representation of a typical melt-pool morphology during LPBF which consists of a solidification front as well as a melting front. As annotated on the solidification front, the magnitude and direction of V_s is a function of location (x, y, z) along the S/L interface. To better understand the evolution of V_s within a 2D microstructure, Figure 12(b) represents the schematic evolution of V_s along the S/L interface within a vertical section of the melt pool around its mid-width. As can be seen, the closer to the top of the melt pool, the higher the V_s. Similarly, within a hori
zontal section (as shown in Figure 12(c)), the closer to the center of the melt pool, the higher the V_s. As pointed out by Qin *et al.*,[2] consistent with the evolution of V_s, the further away from the bottom of the melt pool, the finer the cellular/dendritic structure; *i.e.,* the coarse region forms right next to the MPB and then is gradually refined moving towards the center.

It is well established that, similar to the cell/dendrite spacing, the eutectic lamella spacing is a strong function of cooling rate, thus primarily controlled by V_s (as explained earlier). In the rapid solidification regime, we can obtain an analytical estimation of eutectic lamella spacing as a function of V_s and G for a binary Al-10 wt pct Si system. The assumption of a binary Al-Si system is reasonable considering the small Mg content (~ 0.3 wt pct) in this alloy. Such a low Mg content has a negligible effect on the phase evolution during solidification at the eutectic temperature, *i.e.*, only Al- and Si-rich eutectic lamellae are present at this temperature.

According to Trivedi *et al.*,[28] the relationship between the interface velocity, V_s, and eutectic lamella spacing, λ, can be expressed as

$$V_s\lambda^2 = \phi^2(K_2/K_1), \qquad [1]$$

where $\phi = 3.2$ for Al-Si system. K_2 and K_1 are given by References 28 and 29.

$$K_1 = \bar{m}\frac{\Delta C_0}{D_L}P_e \qquad [2]$$

$$K_2 = 2\bar{m}\left(\frac{\Gamma_{Al}\sin\theta_{Al}}{f_{Al}\left|m^L_{Al}\right|} + \frac{\Gamma_{Si}\sin\theta_{Si}}{f_{Si}\left|m^L_{Si}\right|}\right), \qquad [3]$$

where

$$\bar{m} = \frac{\left|m^L_{Al}\right|\left|m^L_{Si}\right|}{\left|m^L_{Al}\right| + \left|m^L_{Si}\right|}, \qquad [4]$$

$$\Delta C_0 = 2(C_{Si} - C_{Al})(1 - k_v), \qquad [5]$$

$$P_e = 0.335(f_{Al}f_{Si})^{1.65}\frac{2.5\pi/p}{\left[1 + (2.5\pi/p)^2\right]^{1/2} - 1 + 2k_v}, \qquad [6]$$

$$p = \frac{V_s\lambda}{2D_L}, \qquad [7]$$

$$k_v = (k_e + a_0V_s/D_i)/(1 + a_0V_s/D_i). \qquad [8]$$

In the above equations, Γ_{Al} and Γ_{Si} are the Gibbs–Thomson coefficients of the Al and Si phases, respectively, θ_{Al} and θ_{Si}, the contact angles between the solid and liquid, m^L_{Al} and m^L_{Si}, the liquidus line slopes, C_{Si} and C_{Al}, the compositions of the two phases and, f_{Al} and f_{Si}, the volume fractions of the two solid eutectic phases. k_e is the equilibrium partition coefficient and a_0 the atomic jump distance. D_L and D_i are the Si diffusion rates in the liquid and at the liquid and solid interface, respectively. The constants used for current calculations, listed in Table III, were obtained from References 30 and 31.

Equations [1] through [3] are solved numerically, and the variation of eutectic lamella spacing with solidification velocity is plotted in Figure 13(a). As expected, the lamella spacing decreases with solidification velocity which is consistent with the overall decrease in the measured average values of lamella spacing from the coarse to the fine region (*i.e.,* 78.6 nm and 67.8 nm, respectively). It is noteworthy the lamella spacing can be as small as ~ 58 nm at V_s = 2 m/s. Considering a laser scan velocity of 2 m/s as the default machine parameter, the solidification velocity in the fine region can be a maximum of 2 m/s, whereas any location in between the fine region and the MPB can adopt a solidification velocity in the range of 0 to 2 m/s.

B. *Eutectic Volume Fraction*

As with the lamella spacing, the overall volume fraction of eutectic phases appears to decrease from the coarse region towards the fine region, *i.e.*, a reduction from 84.8 ± 0.72 pct to 78.2 ± 0.36 pct (as estimated in Section III–A). This is in contradiction to the prediction of the non-equilibrium lever rule (or Scheil model) for solidification under high cooling rates.[32] Although back diffusion can be neglected under solidification conditions during LPBF (*i.e.*, high V_s and G and thus high cooling rates), the Scheil model is incapable of predicting the effect of a varying cooling rate. Moreover, the Scheil model predicts an increase in the eutectic volume fraction under non-equilibrium solidification conditions, *i.e.*, the worst case scenario is the absence of diffusion in the solid under which the highest fraction of eutectic forms upon solidification.[7] This is contrary to our experimental observations as well as to similar data in the literature obtained for rapid solidification of Al-Si[4,7] and Al-Cu systems.[7]

The shortcomings of the Scheil model are embedded in its inherent assumptions, which are as follows: (1) ignoring dendrite tip undercooling under rapid solidification conditions, and thus (2) the departure from local equilibrium composition and temperature at the tip, as

well as (3) the eutectic temperature depression which changes the maximum solid solubility in the primary α-Al phase. These conditions lead to the reduction in the overall volume fraction of eutectic phase being formed at higher cooling rates in the range of rapid solidification rates. Taking into account the effect of tip undercooling (Burden and Hunt's model[33,34]) as well as the influence of eutectic temperature depression (Jackson and Hunt's model [35]), while also accounting for back diffusion, we can calculate the eutectic volume fraction as a function of V_s. From the derivations by Sarreal and Abbaschian,[7] the variation of eutectic volume fraction f_E^v with the tip undercooling C_t can be expressed as

$$f_E^v = (1 - f_s^\theta)\left[\frac{1}{k_v C_t}\left(C_s^{max} + \frac{A V_s^{1/2}}{m_{Al}^{S(v)}}\right)\right]^{\frac{1}{k_v - 1}} - \frac{2\alpha' k_v}{1 - 2\alpha' k_v}\left(\frac{C_s^{max}}{k_v C_0}\right)^{\frac{(1-2\alpha' k_v)}{k_v - 1}} - \left(\frac{C_s^{max}}{k_v C_0}\right)^{\frac{1}{k_v - 1}}, \quad [9]$$

where

$$f_s^\theta = \frac{C_t - C_0}{C_t(1 - k_v)}, \quad [10]$$

$$C_t = C_0 - \frac{1}{m_{Al}^{L(v)}}\left\{\left[-\frac{8\sigma m_{Al}^{L(v)} T_L^E V_s C_0 (1 - k_v)}{\rho D_L H}\right]^{\frac{1}{2}} + \frac{D_L G}{V_s}\right\}, \quad [11]$$

$$m_{Al}^{L(v)} = \frac{1 - k_v\left(1 - \ln\frac{k_v}{k_e}\right)}{1 - k_e}, \quad [12]$$

$$m_{Al}^{S(v)} = m_{Al}^{L(v)}/k_v \quad [13]$$

$$\alpha' = \alpha\left(1 - e^{-\frac{1}{\alpha}}\right) - \frac{1}{2}e^{-\frac{1}{2\alpha}} \quad [14]$$

$$\alpha = \frac{4 D_s t_f}{\lambda^2} \quad [15]$$

$$t_f = \frac{T_L^S - T_L^E}{\varepsilon} \quad [16]$$

$$\lambda = 4.3\left[\left(T_L^S - T_L^E\right) D_L \Gamma_{Si}/k_v\right]^{1/4} V_s^{-1/4} G^{-1/2}. \quad [17]$$

According to the Scheil model, the volume fraction of eutectic phase for an Al-10 wt pct Si alloy, f_E^s, can be calculated using the following equation[7]:

$$f_E^s = 1 - \left(1 - \frac{C_s^{max}}{k_e C_0}\right)^{\frac{1}{k_e - 1}}. \quad [18]$$

In the above equations, C_s^{max} is the maximum solid solubility of Si in Al at the eutectic temperature, A, a constant and was determined to be $80\text{K} \cdot (\text{s/m})^{1/2}$,[7] $m_{Al}^{L(v)}$ and $m_{Al}^{S(v)}$, the velocity-dependent liquidus and solidus line slopes of the Al phase, C_0, the initial average composition of Si in Al, σ, the solid–liquid interfacial energy, T_L^E, the temperature at the eutectic point, T_L^S, the liquidus temperature at C_0, ρ, the density of the solid, H, the latent heat of fusion, α, the back-diffusion coefficient, D_s, Si diffusion rate in the solid, t_f, the local solidification time, and λ, the interdendritic spacing. It should be noted that, in Eq. [9], k_e, m_{Al}^S , and m_{Al}^L parameters (originally used by Sarreal and Abbaschian[7]) are replaced with the corresponding velocity-dependent values (*i.e.*, k_v, $m_{Al}^{S(v)}$ and $m_{Al}^{L(v)}$) in order to more accurately capture the influence of solidification velocity. The parameters used in the calculations can be found in References 28,30,31,36, and 37 and are listed in Table III.

The estimated volume fraction of eutectic phase is plotted in Figure 13(b) as a function of V_s for a constant G value of 10^6 Km^{-1}. As can be seen in the plot, at slower solidification velocities ($V_s \cong 0.001$ m/s) the eutectic volume fraction increases from the equilibrium value (~ 81 pct) up to a maximum value closer to the prediction by Scheil model (85.08 pct, as calculated using Eq. [18]). The prediction of the Scheil model for the eutectic volume fraction is close to the equilibrium value suggesting a small effect of back diffusion for a high-Si containing Al-Si alloy (*e.g.*, Al-10 wt pct Si) as opposed to a dilute Al-Si alloy (*e.g.*, Al-1 wt pct Si as demonstrated by Sarreal and Abbaschian[7]). The eutectic volume fraction then continuously decreases at higher solidification velocities. It is noteworthy that the measured volume fraction of the eutectic phase in the coarse region is very close to the value predicted by the Scheil model (*i.e.*, 84.8 *vs* 85.08 pct, respectively). Then, in the fine region, it drops to a value (78.2 pct) that is lower than both the equilibrium and Scheil model's prediction. It can thus be suggested that, under the LPBF conditions present in this study, solidification in the fine region enters the rapid solidification regime (*i.e.*, the one which is represented with non-equilibrium conditions at the S/L interface). This is in accordance with the observations of Marola *et al.*[4] indicating a decrease in the eutectic volume fraction of an LPBF-processed AlSi10Mg alloy with respect to the equilibrium value. As mentioned in the preceding section, the solidification velocity in the fine region can be a maximum of 2 m/s where the plot in Figure 13(b) predicts a eutectic volume fraction of ~ 47 pct. However, the average solidification velocity within the sampling areas for the fine region can adopt values well below 2 m/s which may explain the lower volume fraction predicted by the model as compared to that measured by experiment.

C. *Evolution of Precipitates*

The precipitates in the LPBF-produced microstructure in this study consist of two major groups: (1) nano-scale precipitates that appear within the α-Al cells and (2) large precipitates that exist only in the HAZ. The

Table III. Constant Parameters Used for Calculations in this Study

Parameter	Unit	Value	Description
D_L	m^2/s	5.4×10^{-8}	diffusivity of Si in liquid Al
D_i	m^2/s	2.5×10^{-8}	diffusivity of Si in the liquid-solid interface
D_S	m^2/s	8.4×10^{-13}	diffusivity of the solid at T_L^E
Γ_{Al}	m K	1.96×10^{-7}	Gibbs–Thomson coefficients of the Al phase
Γ_{Si}	m K	1.7×10^{-7}	Gibbs–Thomson coefficients of the Si phase
θ_{Al}		30	contact angle between the Si solid and liquid
θ_{Si}		65	contact angle between the Si solid and liquid
f_{Al}	—	0.879	equilibrium volume fraction of the Al solid at the eutectic point
f_{Si}	—	0.121	equilibrium volume fraction of the Si solid at the eutectic point
m_{Al}^L	K/wt pct	− 7.5	liquidus line slope of Al
m_{Si}^L	K/wt pct	17.5	liquidus line slope of Si
C_{Si}	wt pct	1.62	composition of Si in solid at T_L^E
C_{Al}	wt pct	99.98	composition of Si in solid at T_L^E
C_s^{max}	wt pct	1.62	maximum solubility of Si in solid
C_0	wt pct	10	initial composition
T_L^E	K	850	eutectic temperature
T_L^S	K	868	liquidus temperature at T_L^E
k_e	—	0.14	equilibrium partition coefficient
a_0	m	0.5×10^{-9}	atomic jump distance
σ	J/m^2	0.16895	solid–liquid interfacial energy
ρ	kg/m^3	2.35×10^3	density of the solid
A	$K \cdot (s/m)^{1/2}$	80	constant

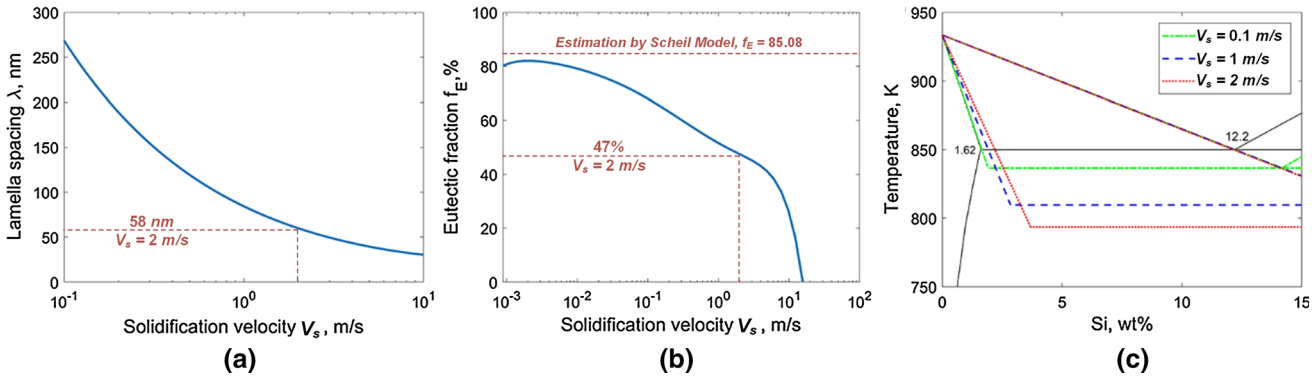

Fig. 13—The variation of (*a*) lamella spacing and (*b*) volume fraction of all eutectic phases as a function of solidification velocity, V_s, in AlSi10Mg alloy. (*c*) The hypo-eutectic portion of Al-Si phase diagram plotted at a variety of V_s values relevant to LPBF processing. Note: the temperature gradient, G, is assumed a constant value of 10^6 Km^{-1} for all calculations.

evolution of precipitates in the HAZ is consistent with that reported in an LPBF-processed AlSi10Mg alloy that is subsequently heat treated.[18,19] Similar to the observations of Li *et al.*[18] for a solution treatment of an LPBF-processed AlSi10Mg alloy at temperatures above 450 °C, the eutectic lamellae structure within the HAZ has dissolved when exposed to high temperatures (*i.e.*, just below the eutectic temperature, ~ 577 °C). Upon subsequent cooling, large irregular-shaped (somewhat spherical) Si-rich particles as well as Mg_2Si phases have then precipitated out of the supersaturated Al matrix.

The nano-precipitates within the α-Al cells, as identified in Section III–B, are predominantly of a Si-rich nature and are either fully or semi-coherent with the Al matrix (see Table II). All variants of nano-precipitates have been observed in both fine and coarse regions, the only difference being an apparent increase in the population of Needle⟨100⟩ precipitates in the coarse region with respect to the fine region. It can be argued that Needle⟨100⟩ may be the more stable variant of nano-precipitates being relatively stabilized by a slower cooling rate within the coarse region. All nano-precipitates (except for spheres and ellipsoids) have been identified with a DC-like superlattice structure which is a non-equilibrium crystal structure as opposed to that of a typical equilibrium Si lattice. This DC-like structure resembles that of a Si network though with a significantly larger lattice constant, *i.e.*, representing a larger crystal unit that in addition to Si contains Al and Mg atoms. Such a non-equilibrium structure, which has not been reported elsewhere so far, is believed to have been developed as a result of high cooling rates during LPBF

Table IV. A Comparison of the Phases Reported in the Literature and Current Study of Al-Mg-Si

Phase	Shape	Formula	Space group	Lattice parameters (pm)	References
β''	needle	Mg_5Si_6	monoclinic, C2/m	$a = 1516$, $b = 405$, $c = 674$, $\beta = 105.3$ deg	39,40
β'	needle	$Mg_{1.8}Si$	hexagonal, $P6_3/m$	$a = b = 715$, $c = 405$, $\gamma = 120$ deg	43,44
U1	needle	$MgAl_2Si_2$	trigonal, $P_{\bar{3}ml}$	$a = b = 405$, $c = 674$, $\gamma = 120$ deg	38
U2	needle	MgAlSi	orthorhombic, P_{nma}	$a = 675$, $b = 405$, $c = 794$	42
B'	lath	$Mg_9Al_3Si_7$	hexagonal, $P6_3/m$	$a = b = 1040$, $c = 405$, $\gamma = 120$ deg	41
β	plate/cube	Mg_2Si	cubic, $F_{m\bar{3}m}$	$a = 635.4$	43
Pure Si	plate	Si	cubic, F_{d3m}	$a = 543.1$	
Al-Si	needle/plate	Al_xSi_{1-x}	cubic, F_{d3m}	$a = 1214$	current study

of AlSi10Mg alloy. Also, many of these precipitates were identified with partially or fully distorted lattice structures (see Figure 10) which, again, is likely a direct result of high cooling rates. In other words, the distortion or fault found within the precipitates can be the result of accommodation of the lattice strains occurring during rapid solidification and subsequent fast cooling of supersaturated α-Al cells. It has been reported that the precipitation sequence in Al-Mg-Si alloys upon aging is as follows[38]:

$$\text{Atomic clusters} \rightarrow \text{GP zones} \rightarrow \beta'' \rightarrow \beta', \text{ U1, U2, } B' \rightarrow \beta, \text{ Si.}$$

Each of the phases has a distinct crystal structure, atom arrangement, lattice parameter and composition, which is summarized in Table IV. With careful comparison with the diffraction patterns and composition, none of the identified phases in the current study belongs to the any of the previous identified ones in the literature.[38–44] The needle⟨100⟩, needle⟨110⟩, and needle⟨112⟩ precipitates have a diamond cube superlattice crystal structure and contain mainly Al and Si. However, the detailed composition and atom arrangement needs to be further investigated in a separate study.

The supersaturation of α-Al cells can be explained by referring to the non-equilibrium phase diagram of Al-Si plotted as a function of solidification velocity in Figure 13(c). The non-equilibrium phase diagram is constructed using velocity-dependent values of liquidus line slope, $m_{Al}^{L(v)}$, and partition coefficient, k_v, in Eq. [11] and plotting the change in the solid and liquid tip compositions by temperature. The plots show that, at solidification velocities that are relevant during LPBF in this study (up to 2 m/s), the solubility limit can shift to significantly larger Si concentrations (*i.e.*, ~ 3.5 wt pct Si at $V_s = 2$ m/s, as opposed to the equilibrium value of 1.62 wt pct Si). This gives rise to the solidification of highly saturated α-Al cells within which non-equilibrium Si-rich precipitates can form after solidification, *i.e.*, upon fast cooling down below the eutectic temperature. As Marola *et al.*[4] also pointed out, the fast cooling in solid state (following solidification) is the characteristic of LPBF processing which is caused by the direct contact between the solidifying melt pool and the cold, solid layer underneath it. There are also large and highly Si-rich (close to 100 wt pct Si) particles forming along the cell boundaries, such as those observed in Figure 5(b_2). Such inter-cellular particles may represent a discontinuous/fibrous version of the Si eutectic phase that has been reported to likely form at highly non-equilibrium solidification conditions, such as in LPBF.[1,4,45]

It should be also noted that, in addition to the precipitation upon cooling from solidification temperatures, there is also the possibility of occurrence of precipitation within the supersaturated α-Al matrix during the subsequent thermal cycles. However, it is not possible to distinguish the formation of nano-precipitates due to post-solidification cooling from those that might form due to the thermal cycles from the subsequent tracks/layers during a continuous 3D printing process. This is because we can only study the final microstructure. However, the highly non-equilibrium nature of these precipitates (*i.e.*, in terms of morphology, Si concentration, and crystal structure) may be indicative of a very fast cooling rate which is more likely to occur right after solidification rather than due to the subsequent thermal cycles. To more accurately separate the microstructural manifestation of these two phenomena, more in-depth analysis of thermal cycles during the LPBF process is necessary (*i.e.*, to know what thermal history the solidified microstructure will be exposed to and whether the temperatures/times are high enough to trigger any precipitation phenomenon).

D. *Nano-hardness Evolution*

Figure 14 shows nano-indentation results across the top-view section of a solidified melt pool. The measurements were performed along six linear passes across the width of the melt pool, as can be seen in Figure 14(a). As shown in Figure 14(b), overall, all measurement lines exhibit the same hardness profile with a maximum value occurring around the melt-pool centerline. Together with the evolution of cellular structure around and away from the MPB (as shown in Figure 14(c)), it can be suggested that the HAZ exhibits the lowest, the coarse zone the intermediate, and the fine zone the highest hardness across the microstructure. This is consistent with the quantitative as well as the qualitative evolution of the cellular/dendritic structure, eutectic phase, and nano-precipitates, as identified and explained in the preceding sections. The cellular/dendritic structure, eutectic phases, and nano-precipitates have largely vanished in the HAZ where the microstructure predominantly consists of a low population of large precipitates

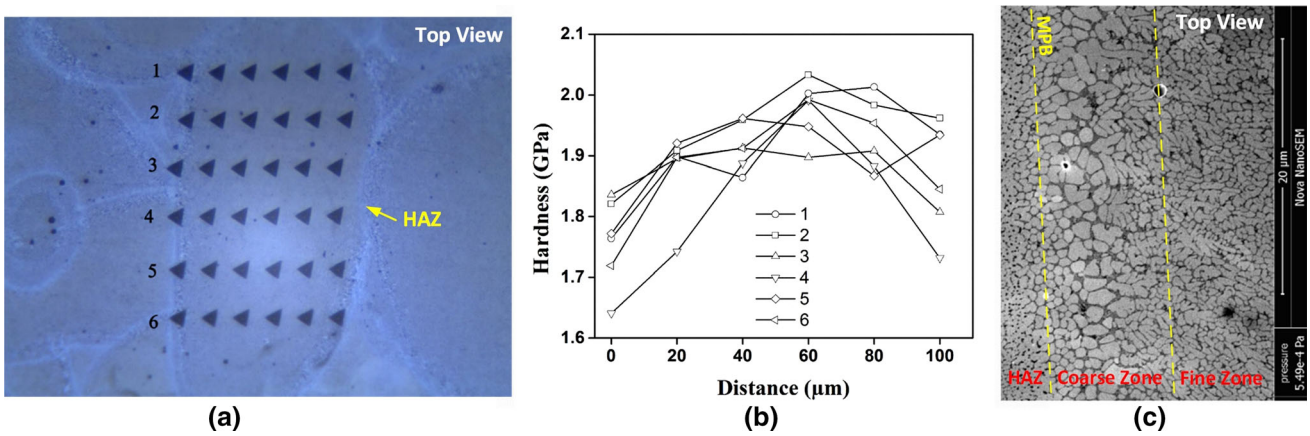

Fig. 14—(*a*) The indentation marks and (*b*) the variation of nano-hardness across a solidified melt pool in a cross-sectional view along the top-view direction. (*c*) The SEM images showing the corresponding variation of microstructure across the HAZ, the coarse, and the fine zone.

and broken-up eutectic phases. Such a microstructural difference may explain a significantly lower hardness in the HAZ, *i.e.*, ~ 75 pct of the measured peak hardness within the solidified melt pool. The hardness profiles show a relatively sharp increase as the indent shifts into the coarse region. This is consistent with the existence of cell boundaries, eutectic phases, and nano-precipitates in the coarse region as opposed to only large precipitates in the HAZ. The hardness consistently increases as the indent shifts further towards the centerline region. This can be explained by the corresponding refinement of cellular/dendritic structure and the eutectic lamellae. However, the simultaneous reduction in the volume fraction of eutectic phases as the indent moves into the fine region may have a negative effect on the hardness. One can argue that such a negative effect is overcome by the larger positive contribution from the microstructural refinement.

The nano-precipitates identified in this study appear in large number densities and possess either a fully or semi-coherent interface with the Al matrix. Moreover, many of them have either partially or fully distorted lattices. We can thus expect nano-precipitates to have a considerable contribution to the overall hardness. The degree to which each of the strengthening agents (namely, cell boundaries, eutectic phases, and nano-precipitates) contributes to the overall hardness will be investigated in the future. Moreover, with the peak hardness being along the centerline of each track, there exists a periodical variation of hardness across the build, *i.e.*, with a wavelength of the size of the track width and an amplitude of ~ 25 pct of the peak hardness (according to the profiles shown in Figure 14(b)). The effect of processing conditions on such local hardness variations and thus the bulk mechanical properties has yet to be investigated.

V. CONCLUSIONS

Utilizing advanced experimental and analytical electron microscopy techniques, together with analytical modeling of rapid solidification phenomenon, we unveiled the complex, non-equilibrium phase evolution in an as-built LPBF-processed AlSi10Mg alloy. The evolution of strengthening agents such as the inter-cellular eutectic phases and intra-cellular precipitates is presented in correlation with the local variations of solidification conditions and thus with the corresponding evolution of cellular/dendritic patterns within a typical melt pool. We conclude that

1. The eutectic phase exhibits lamellar and fibrous morphology across the solidified microstructure, *i.e.*, within the cell boundaries in coarse and fine cellular/dendritic zones. The volume fraction of eutectic phases and the lamella spacing is shown to gradually decrease as moving away from the melt-pool boundary, *i.e.*, upon crossing over from a coarse to a fine cellular zone. This is in correlation with the cell size variation suggesting an all-inclusive microstructural refinement away from the melt-pool boundary towards the melt-pool centerline.
2. The eutectic-free regions within the α-Al cells contain a large number density of nano-sized precipitates that are predominantly Si-rich. These nano-precipitates are either fully or semi-coherent with the Al matrix, the formation of which may be linked to the increased solubility limits of α-Al cells with respect to the equilibrium value, *i.e.*, due to the rapid solidification effect.
3. For the first time, we identified such nano-precipitates with non-equilibrium crystal structures and morphologies induced by high cooling rates. "Spheres" and "Ellipsoids" possess the same (FCC) crystal structure as of the Al matrix though being slightly distorted. "Plates" and all variants of "Needles" exhibit a DC superlattice crystal structure that emerges from within the Al matrix. Needles, however, appear with three different orientations (needle⟨112⟩, needle⟨110⟩, and needle⟨100⟩) each one holding a distinct orientation relationship with the Al matrix. Moreover, both plates and needles also appear with partially or fully distorted/irregular crystal structures.

4. The microstructure in the HAZ (right underneath the MPB) exhibits an absence of cell boundaries and eutectic phases while consisting primarily of large Si-rich and Mg-rich precipitates. The HAZ microstructure and phase evolution seem to resemble that of a solution-treated AlSi10Mg alloy after LPBF processing.
5. The local variation of nano-hardness (*i.e.*, across a solidified melt pool) is shown to correspond well with the microstructural refinement profile, *i.e.*, exhibiting the minimum at the HAZ and the peak at around the melt-pool centerline.

The above findings shed significant light on the evolution mechanisms of major strengthening agents in AlSi10Mg, including the fully or partially coherent nano-precipitates, fine eutectic phases, and cell boundaries. We showed that the evolution of such features is predominantly determined by the local solidification conditions within each melt pool, *i.e.*, the solidification velocity, which itself is controlled by the LPBF processing variables. These microstructural strengthening agents collectively control the local strength and its variation across the microstructure as well as the bulk mechanical properties of an as-built, LPBF-processed AlSi10Mg alloy. The extent to which each one of these agents contributes to the overall strength has yet to be studied. The new knowledge presented here can be effectively utilized in LPBF process optimization for microstructural enhancement and mechanical performance.

ACKNOWLEDGEMENTS

This research was supported by the NSERC Discovery Grant program and the Queen's University Faculty of Engineering and Applied Science Dean's Research Fund. We are grateful for the useful discussions with Dr. Mark Gallerneault that took place during the course of this work.

REFERENCES

1. A. Hadadzadeh, B.S. Amirkhiz, J. Li, A. Odeshi M. Mohammadi: *Mater. Sci. Eng. A*, 2018, vol. 722, pp. 263–68.
2. H. Qin, V. Fallah, Q. Dong, M. Brochu, M.R. Daymond, and M. Gallerneault: *Mater. Charact.*, 2018, vol. 145, pp. 29–38.
3. L. Thijs, K. Kempen, J.-P. Kruth, and J. Van Humbeeck: *Acta Mater.*, 2013, vol. 61, pp. 1809–19.
4. S. Marola, D. Manfredi, G. Fiore, M.G. Poletti, M. Lombardi, P. Fino, and L. Battezzati: *J. Alloys Compd.*, 2018, vol. 742, pp. 271–79.
5. M. Tang, P.C. Pistorius, S. Narra, and J.L. Beuth: *JOM*, 2016, vol. 68, pp. 960–66.
6. V. Fallah, D.J. Lloyd, and M. Gallerneault: *Mater. Sci. Eng. A*, 2017, vol. 698, pp. 88–97.
7. J.A. Sarreal and G.J. ABbaschian: *Metall. Trans. A*, 1986, vol. 17A, pp. 2063–73.
8. Y.E. Kalay, L.S. Chumbley, I.E. Anderson, and R.E. Napolitano: *Metall. Mater. Trans. A*, 2007, vol. 38A, pp. 1452–57.
9. J.D. Roehling, D.R. Coughlin, J.W. Gibbs, J.K. Baldwin, J.C.E. Mertens, G.H. Campbell, A.J. Clarke, and J.T. McKeown: *Acta Mater.*, 2017, vol. 131, pp. 22–30.
10. Z. Xiong, S. Liu, S. Li, Y. Shi, Y. Yang, and R. Misra: *Mater. Sci. Eng. A*, 2019, vol. 740, pp. 148–56.
11. N. Read, W. Wang, K. Essa, and M.M. Attallah: *Mater. Des.*, 2015, vol. 65, pp. 417–24.
12. K. Kempen, L. Thijs, J. Van Humbeeck, and J.-P. Kruth: *Phys. Procedia*, 2012, vol. 39, pp. 439–46.
13. E. Brandl, U. Heckenberger, V. Holzinger, and D. Buchbinder: *Mater. Des.*, 2012, vol. 34, pp. 159–69.
14. D. Buchbinder, H. Schleifenbaum, S. Heidrich, W. Meiners, and J. Bültmann: *Phys. Procedia*, 2011, vol. 12, pp. 271–78.
15. T.G. Holesinger, J.S. Carpenter, T.J. Lienert, B.M. Patterson, P.A. Papin, H. Swenson, and N.L. Cordes: *JOM*, 2016, vol. 68, pp. 1000–11.
16. E. Louvis, P. Fox, and C.J. Sutcliffe: *J. Mater. Process. Technol.*, 2011, vol. 211, pp. 275–84.
17. E. Olakanmi: *J. Mater. Process. Technol.*, 2013, vol. 213, pp. 1387–1405.
18. W. Li, S. Li, J. Liu, A. Zhang, Y. Zhou, Q. Wei, C. Yan, and Y. Shi: *Mater. Sci. Eng. A*, 2016, vol. 663, pp. 116–25.
19. N.T. Aboulkhair, C. Tuck, I. Ashcroft, I. Maskery, and N.M. Everitt: *Metall. Mater. Trans. A*, 2015, vol. 46A, pp. 3337–41.
20. J.H. Rao, Y. Zhang, K. Zhang, A. Huang, C.H. Davies, and X. Wu: *Scripta Mater.*, 2019, vol. 160, pp. 66–69.
21. V. Fallah, A. Korinek, B. Raeisinia, M. Gallerneault S. Esmaeili: *Mater. Sci. Forum*, 2014, vols. 794–796, pp. 933–38.
22. V. Fallah, A. Korinek, N. Ofori-Opoku, B. Raeisinia, M. Gallerneault, N. Provatas, and S. Esmaeili: *Acta Mater.*, 2015, vol. 82, pp. 457–67.
23. V. Fallah, B. Langelier, N. Ofori-Opoku, B. Raeisinia, N. Provatas, and S. Esmaeili: *Acta Mater.*, 2016, vol. 103, pp. 290–300.
24. V. Fallah, A. Korinek, N. Ofori-Opoku, N. Provatas S. Esmaeili: *Acta Mater.*, 2013, vol. 61, pp. 6372–86.
25. V. Fallah, A. Korinek, N. Ofori-Opoku, N. Provatas S. Esmaeili: *Acta Mater.*, 2015, vol. 2015, pp. 470–72.
26. V. Fallah, M. Alimardani, S.F. Corbin, and A. Khajepour: *Comput. Mater. Sci.*, 2011, vol. 50, pp. 2124–34.
27. V. Fallah, M. Amoorezaei, N. Provatas, S. Corbin A. Khajepour: *Acta Mater.*, 2012, vol. 60, pp. 1633–46.
28. R. Trivedi, F. Jin, and I.E. Anderson: *Acta Mater.*, 2003, vol. 51, pp. 289–300.
29. W. Kurz and R. Trivedi: *Metall. Trans. A*, 1991, vol. 22A, pp. 3051–57.
30. L.M. Hogan and H. Song: *Metall. Mater. Trans. A*, 1987, vol. 18, pp. 707–13.
31. D.M. Stefanescu: *Science and Engineering of Casting Solidification*, Springer, New York, 2015.
32. M.C. Flemings: *Metall. Trans.*, 1974, vol. 5, pp. 2121–34.
33. M.H. Burden and J.D. Hunt: *J. Cryst. Growth*, 1974, vol. 22, pp. 99–108.
34. M.H. Burden and J.D. Hunt: *J. Cryst. Growth*, 1974, vol. 22, pp. 109–16.
35. J. Hunt and K. Jackson: *Trans. Metall. Soc. AIME.*, 1966, vol. 236, pp. 843–52.
36. M. Gündüz and J.D. Hunt: *Acta Metall.*, 1985, vol. 33, pp. 1651–72.
37. S.-I. Fujikawa, K.-I. Hirano, and Y. Fukushima: *Metall. Trans. A*, 1978, vol. 9A, pp. 1811–15.
38. S.J. Andersen, C.D. Marioara, R. Vissers, A. Frøseth, and H.W. Zandbergen: *Mater. Sci. Eng. A*, 2007, vol. 444, pp. 157–69.
39. H.W. Zandbergen, S.J. Andersen, and J. Jansen: *Science*, 1997, vol. 277, pp. 1221–25.
40. S.J. Andersen, H.W. Zandbergen, J. Jansen, C. TrÆholt, U. Tundal, and O. Reiso: *Acta Mater.*, 1998, vol. 46, pp. 3283–98.
41. K. Matsuda, Y. Sakaguchi, Y. Miyata, Y. Uetani T. Sato, A. Kamio, and S. Ikeno: *J. Mater. Sci.*, 2000, vol. 35, pp. 179–89.

42. S.J. Andersen, C.D. Marioara, A. Frøseth, R. Vissers, and H.W. Zandbergen: *Mater. Sci. Eng. A*, 2005, vol. 390, pp. 127–38.
43. M.H. Jacobs: *Philos. Mag.*, 2006, vol. 26, pp. 1–13.
44. R. Vissers, M.A. van Huis, J. Jansen, H.W. Zandbergen, C.D. Marioara, and S.J. Andersen: *Acta Mater.*, 2007, vol. 55, pp. 3815–23.
45. M. Liu, N. Takata, A. Suzuki, and M. Kobashi: *Mater. Des.*, 2018, vol. 157, pp. 478–91.